Chapter 2
Features of Stiff Vacuum Extrusion as a Method of Briquetting Natural and Anthropogenic Raw Materials

Stiff vacuum extrusion (SVE) technology is applied in the production of ceramic bricks in 64 countries around the world, including the United States, Britain, Germany, South Korea, and South Africa. The world's largest brick factory in Saudi Arabia produces a million bricks per day using SVE technology [1].

In accordance with brick industry terminology, the word "stiff" is used to describe the process of extrusion, which is carried out at pressures ranging from 2.5 to 4.5 MPa and moisture contents ranging from 12 to 18% (Table 2.1 [2]).

2.1 Preparation of Burden Materials for SVE Briquetting

One of the basic criteria determining the suitability of extrusion material is its plasticity—a trait that assures that it can be effectively pushed through the holes in die. A necessary condition for the status of plasticity is complying with the granulometric composition and moisture content requirements for SVE. In some cases, additional pulverization may be required in order to achieve the desired plasticity of material.

Unlike a roller press and vibropress briquetting, shear stress plays an important role in SVE agglomeration. Shear stress occurs when the mixture is processed in the screw feeder, in pug mills, and then in the extruder. In [3], based on a comparison of coal briquette porosity values in various pressing options (compression and its combination with torsion), it was found that more dense briquettes (less porous) are formed in the combined pressing option (under identical values of applied pressure). With full compression, a significant proportion of energy is expended on the elastic deformation of the particles themselves, while, in the presence of shear stress, the convergence of particles on the surface forces activation distance is more effective. In full compression of close-packed particles, each particle only comes into contact with its immediate neighbors and is subjected to a compression load. Under shear stress, the particles of the adjacent layers are subjected to abrasion due

I. Kurunov and A. Bizhanov, *Stiff Extrusion Briquetting in Metallurgy*,
Topics in Mining, Metallurgy and Materials Engineering,
https://doi.org/10.1007/978-3-319-72712-7_2

Table 2.1 Types of extrusion

Type of extrusion	Low-pressure extrusion	Medium-pressure extrusion	High-pressure extrusion	
Designation used in structural ceramic industry	Soft extrusion	Semi-stiff extrusion	Stiff extrusion	
Extrusion moisture, % on dry	10–27	15–22	12–18	10–15
Extrusion pressure, MPa	0.4–1.2	1.5–2.2	2.5–4.5	Up to 30

to contact with irregular surfaces, which can lead to crushing, the opening up of new surfaces, and, hence, to an increase in the number of contacts between particles of the mixture.

In order to identify the possible impact of shear stress on the change of particle size distribution of briquetted material in conditions of SVE, we have compared the results of pulverization of coke fines in three different ways: in a hammer mill, in a roller crusher, and by double shearing through shearing plate in the extruder (Fig. 2.1). Samples of original coke breeze had the following properties: 8.97% moisture content; 13.28% ash content; volatile content 3.45%; 0.61% sulfur content. Since coke breeze particle was larger in size than what is usually required for extrusion, they were pulverized.

Fig. 2.1 Equipment and tools for materials pulverization (top left—hammer mill; top right-roller crusher; bottom left—shearing through the shearing plate of extruder; bottom right—shearing plate)

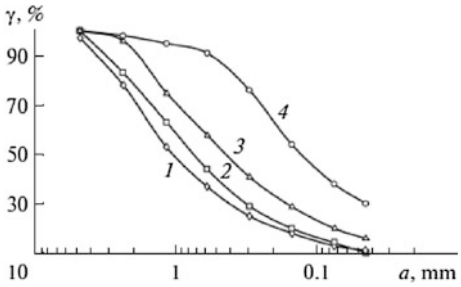

Fig. 2.2 Granulometric composition of coke breeze in the following states: (1) initial and (2–4) after additional grinding in a hammer mill, in a roll crusher, and double extrusion in an extruder, respectively. γ is the yield of the oversize mass, and a is the mesh size

Wet screens were used to determine particle size distributions of raw materials. Moisture content was measured using a moisture balance. A calibrated electronic scale with a density measuring attachment was used to determine pellet density. The results of the granulometric analysis are presented in Fig. 2.2.

As evidenced above, the grinding of coke breeze is maximized after double extrusion through a shearing plate in an extruder. In this case, the effect of deep grinding is achieved through the application of high shear stresses. The use of a hammer mill for such a material was found to be ineffective, and the granulometric composition of the ground material differed weakly from that of the initial coke breeze.

Based on these results, we decided to study the effects of the grinding method on the strength of the brex produced from coke breeze pulverized in different manners. Three portions of brex of the same composition—94% of coke breeze, 5% of Portland cement, and 1% bentonite—were manufactured. The only difference between the brex was the manner in which the coke breeze was ground. The brex were classified assigned the following numbers in accordance with the method of grinding: No. 1 was coke breeze ground by roller crusher; No. 2 was coke breeze sheared twice through the shearing plate with a plurality of holes; No. 3 was coke breeze ground by hammer mill. Extrusion parameters and physical properties of brex are shown in Table 2.2.

It follows from these data that the extrusion of the first two mixtures was carried out in accordance with similar processing parameters and that the extrusion of the coarser particles in mixture No. 3 (hammer mill) is accompanied by an increase in the temperature of the material. As a result, the brex made of the largest particles turned out to have the minimum strength in axial compression tests. As for energy consumption, the extrusion of mixture No. 1 was most efficient. Its excellent extrusion ability can be attributed to the material particle shape after grinding in a roll crusher, which favors the plane-parallel orientation of particles.

The difference between the tensile strengths of samples No. 1 and No. 2 is insignificant and only indicates an earlier beginning of cracking in brex No. 2. It also follows from this data that the density of brex after double extrusion exceeds

Table 2.2 Extrusion parameters and physical properties of coke breeze brex

Sample of brex (grinding method)	Moisture content, %	Temperature °C	Vacuum, mm Hg.	Density, g/cm^3	Compressive strength, kgf/cm^2
No. 1 (roller crusher)	16.5	30.56	15.24	1.63	37.76
No. 2 (double shearing)	16.7	33.33	17.78	1.67	34.32
No. 3 (hammer mill)	16.6	55.56	81.28	1.63	20.25

that of brex samples made of ground and milled coke breeze by 2.5%. Obviously, the dense packing of brex No. 2 particles is the result of a high degree of material grinding. In contrast to brex samples No. 1 and No. 3, no mixture dewatering was detected during extrusion in this case. Differences in compressive strengths of brex samples prepared from differently treated coke breeze of the same batch—can result from a number of factors related to different particle sizes, shapes, and surface relief. The shape of a particle after grinding depends on material characteristics and the grinding method, including time [4–6]. For example, it is generally accepted that, after grinding in roll crushers, the material mainly consists of angular particles, whereas the material particles usually maintain the same size and a rounded shape after ball and hammer milling. In roll crushers, grinding occurs under the compressive, shear, and rubbing forces. As a result, you have rough particles with sharp projections, many edges and corners, and (correspondingly) a large contact surface form. When the material is ground by hammer mill, the particle surfaces are polished by way of impact and the particles acquire a rounded shape.

For example, the researchers [7] studied the effect of grinding device on oil coke particle shape of (1) low-porosity coke with thick cell walls without visible cracks and (2) fissured coke whose porosity and cell wall thickness of which were distributed over a wide range. In the first instance, grinding method did not affect the shape of particles 200–600 μm in size. In the second instance, it was revealed that the particle shape is dependent on particle size in various ways when ground in a hammer mill and in a roll crusher (Fig. 2.3) [7].

These curves reflect the following dependence of the shape factor: $\phi = 1.1V1/3N1/6A-1/2$, where V is the specific particle volume (cm^3/g), N is the number of particles in 1 g substance, and A is the specific surface area (cm^2/g). The material particles ground in a hammer mill are characterized by stable high shape factors, which indicate the closeness of most of the particles' forms to a rounded shape in

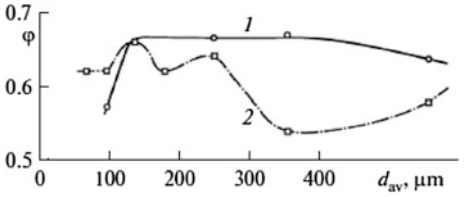

Fig. 2.3 Particle shape factor ϕ versus the average particle size upon grinding in (1) hammer mill and (2) roll crusher [7]

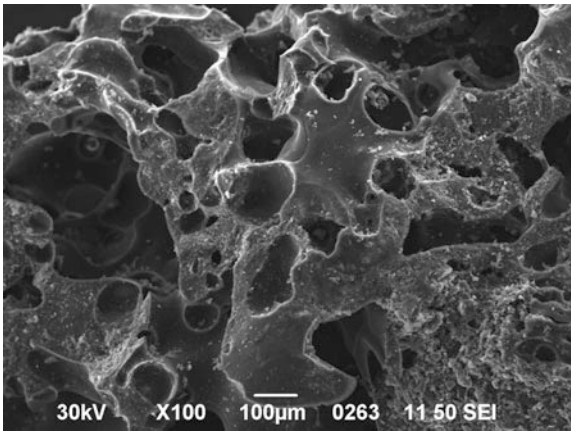

Fig. 2.4 Structure of coke breeze particle (scanning electron microscopy)

the indicated size range. For the particles of the material ground in a roll crusher, the shape factors in the 140–600 μm particle size range are lower and minimal at a size of ~350 μm, which supports the conclusion about a more nonuniform particle shape after grinding in a roll crusher.

As in [7], we used a porous and fissured material. Figure 2.4 shows an image of coke breeze particles taken with a JEOL JSM_6490 LV scanning electron microscope (SEM). In Fig. 2.5, we compare the particle shapes of the initial coke breeze and the coke breeze after additional grinding. The initial coke breeze particles are characterized by hillocks (rounded projections), which are typical of coke; they belong to internal (not opened) pores located under the upper layers of the carbon material. It is seen that the particles after a roll crusher and double extrusion through an extruder have a nonuniform angular shape, whereas the coke breeze particles ground in a hammer mill have a rounded shape.

The brex samples were subjected to tensile splitting tests on a bench-type one-column electromechanical Instron 3345 tensile testing machine at a load of 5 kN. When studying the statistics of brex orientation distribution in a charge, we [8, 9] found that this type of external load is most probable for a cylindrical brex. Figure 2.6 shows the results of testing specially prepared cylindrical specimens of brex 1–3 25 mm in diameter and 20 mm in height. It is seen that, at approximately the same carrying ability, the brex specimens' reactions to an applied load are different.

The difference in the maximum loads can be related to defects in the specimens. However, the difference in the characters of behavior can have radically different causes. Brex No. 2 demonstrates ductile fracture, which is indicated by the existence of a yield plateau, i.e., the horizontal component of the brex No. 2 curve. This phenomenon is thought to be explained by a "relay-race" grain to grain gliding transfer in accordance with the Hall–Petch equation stipulating an inverse relationship between grain size and yield strength [10]. In this case, a grain boundary is a barrier to dislocation motion, which causes dislocation nucleation and development

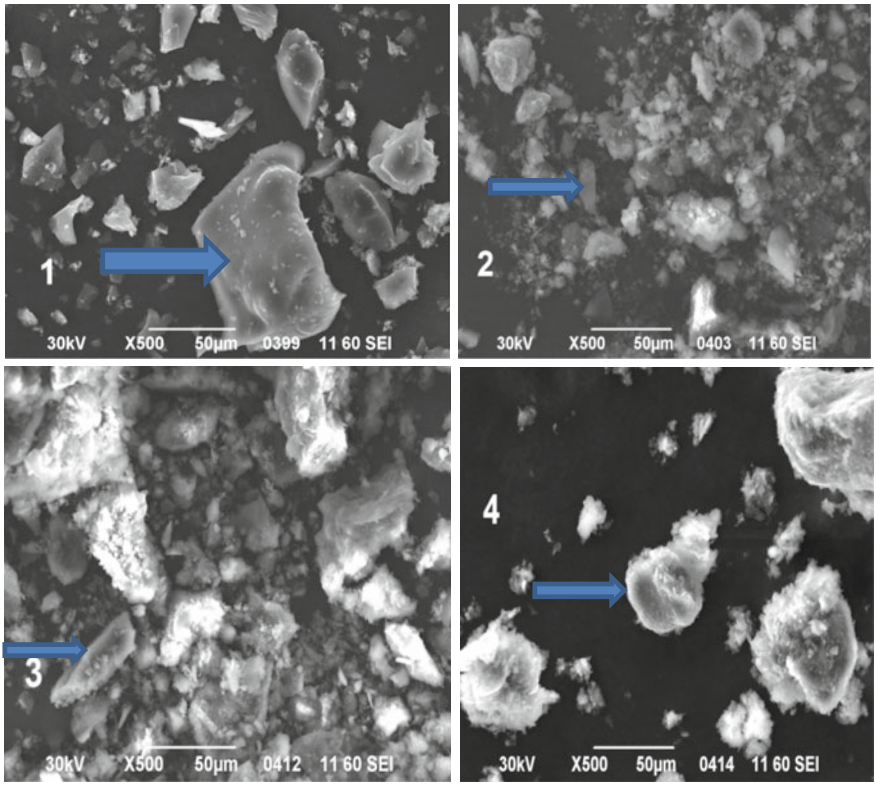

Fig. 2.5 Micrographs of (1) initial coke breeze particles and after additional grinding, (2) in roll crusher, (3) by double extrusion through an extruder, and (4) in a hammer mill

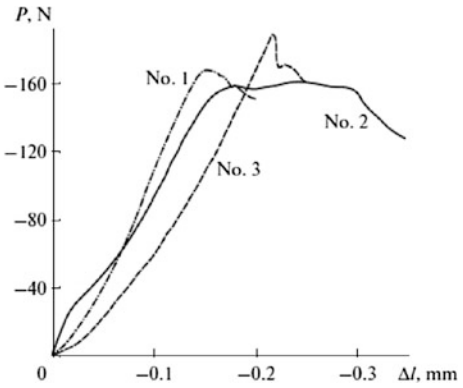

Fig. 2.6 Load P-displacement Δl curves for cleavage tensile tests of brex

in a neighboring grain. In other words, the larger the number of barriers to be overcome, the lower the dislocation motions dynamics and the higher the crack development resistance.

Apparently, there exists a threshold particle size, below which cracks cannot propagate in brex. Obviously, the granulometric composition of the brex No. 2 mixture favors this scenario due to the highest content of thin particles among the other mixtures (see Table 2.2). The integrity of brex No. 2 is retained even after tests; therefore, high impact strength can be expected. At this type of loading, local fracture zones will not cause full fracture and debris formation in a specimen. The load–displacement curves of brex No. 1 and No. 3 decrease significantly after crack initiation, which points to more brittle fracture of these specimens. The brittle fracture in brex No. 1 develops more slowly than it does in brex No. 3 because of a smaller average particle size. Note that these circumstances are very important for briquetting. Several stages of charging–discharging related to throwing down briquettes can be required to supply the briquettes to a furnace even in one enterprise. When the impact toughness of an agglomerated product is increased, the logistics of supplying it to the site, including those that are far away, can be significantly simplified and, hence, be made cheaper. It is important for stiff extrusion that a change in the behavior of brex under external mechanical action was achieved using same agglomeration equipment.

In addition to the physical mechanisms that weaken dislocation propagation, leading to a high strength of brex made of small particles, the distribution of a binder in the brex body also substantially contributes to its strength. It is clear that the low strength of brex No. 3 during compression can be explained by a small amount of contacts between particles. Figure 2.7 shows micrographs of the particle surfaces in brex No. 3 (grinding in a hammer mill) and brex No. 2 (double extrusion through a shearing plate). It is clearly visible that, because of the lower particle surface roughness of brex No. 3 as compared to brex No. 2, the number of hillocks with a binder (cement and bentonite) on their surface (bright aggregates) is significantly lower. (Since minerals contain heavy chemical elements, they manifest themselves as bright precipitates in micrographs.) Therefore, the surface relief of the brex No. 2 particles also favors good adhesion of particles due to the large binder volume that covers the sites of particle–particle contacts.

When studying the particle surfaces of brex No. 2, we detected bentonite fibers, which were described for the first time in [11]. Figure 2.8 shows the surface of brex No. 2 particle and the surfaces of glass microspheres subjected to soft rolling (without crashing) in a roll crusher which imitated shear stresses. This treatment promoted the development of bentonite fibers covering the particle surface. After this preliminary treatment of a magnetite concentrate and bentonite mixture, the fraction of bentonite required for the given strength decreased twofold (from 0.66 to 0.33% concentrate mass). The appearance of this structure in brex No. 2 is likely to result from the shear stress applied to the material during auger extrusion. The effect of the appearance of bentonite fibers is less pronounced in brex No. 1 and No. 3, which is likely to be associated with a lower fraction of thin particles. Brex No. 1 and No. 3 have predominantly lamellar and flake-like bentonite particles (Fig. 2.9).

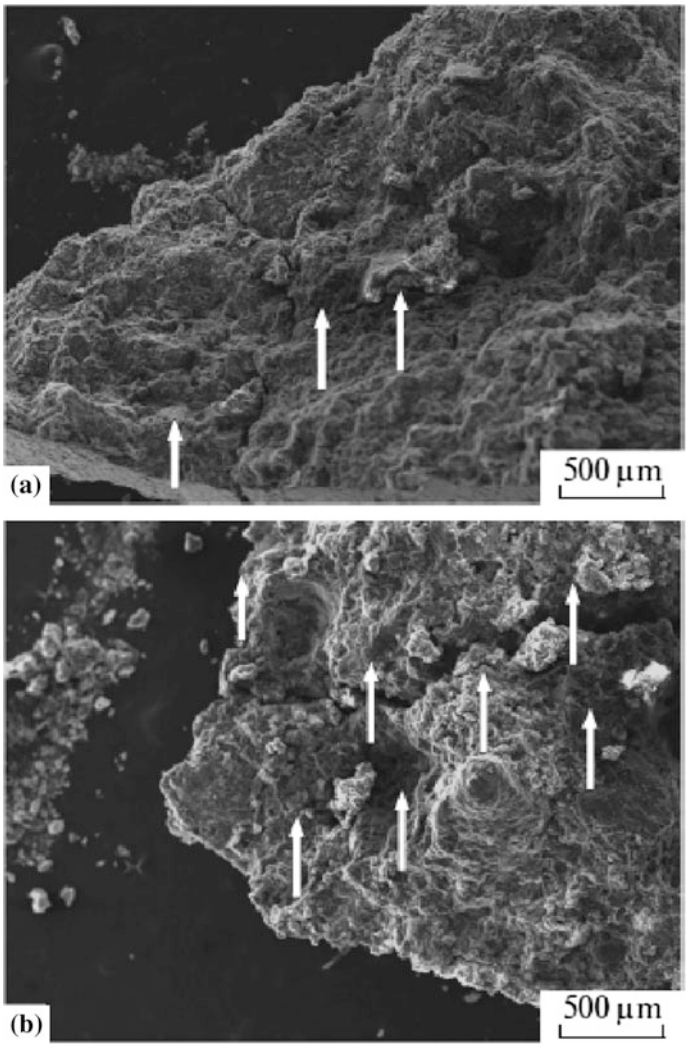

Fig. 2.7 SEM micrographs of the particle surfaces in brex No. 3 (**a**) and No. 2 (**b**)

A mixture becomes suitable for extrusions through the addition of a plasticizing agent, mainly bentonite, to a charge. The fraction of bentonite required to ensure the extrusion of a mixture oscillates in the 0.25–1.0% range of the briquetted material density. An important consequence of the plasticized mixture is an increase in the mechanical strength of brex and a change in the character of its fracture from brittle to viscoplastic fracture.

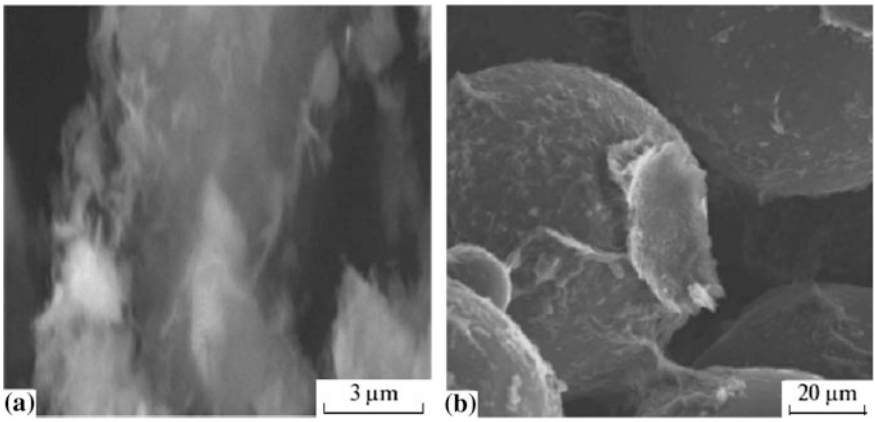

Fig. 2.8 Bentonite fibers on **a** the particle surface in brex No. 2 and **b** on the surface of glass microspheres [11]

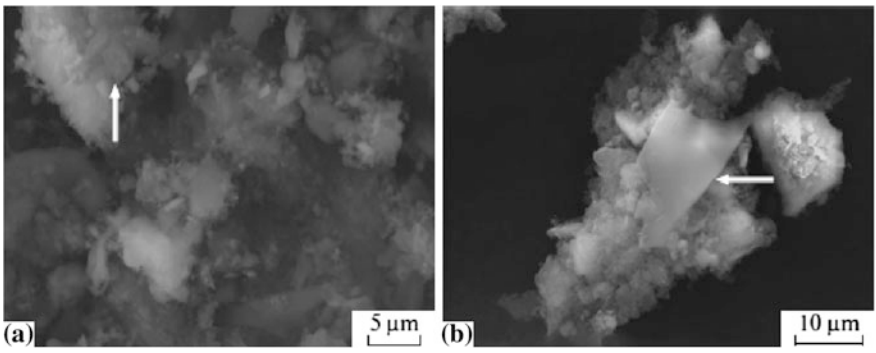

Fig. 2.9 Bentonite particles in brex No. 1 (**a**) and No. 3 (**b**)

Below, we present axial compression test results of first series brex made of a charge of a base composition of 67% dust of the aspiration of ferrochrome production, 15% chromium ore concentrate, 15% coal, 3% Portland cement, and second series brex made of the same charge with an addition of 0.5% bentonite that were performed in a laboratory extruder. The axial compression tests of the brex of both series were carried out on a bench-type one-column electromechanical Instron 3345 tensile testing machine at a load of up to 5 kN. Figure 2.10 shows the stress–strain curves that demonstrate the change in the character of fracture of bentonite-containing brex from pronounced brittle to viscoplastic fracture. This change is also illustrated in Fig. 2.11, which shows that in the case of fracture of bentonite-containing brex, the compression surfaces of the tensile testing machine should be much closer than they are in the case of bentonite-free brex. A comparison of the strengths of the brex of two series showed that the average

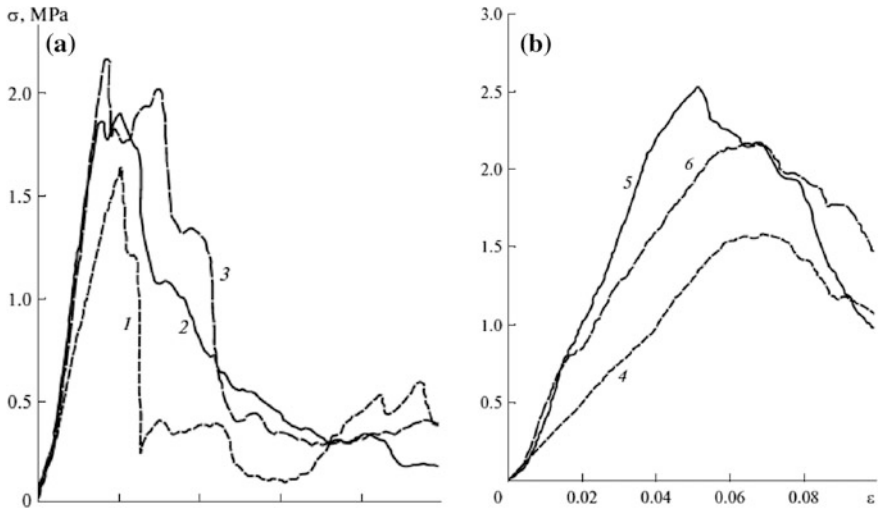

Fig. 2.10 Stress σ–strain ε curves for brex based on aspiration dust **a** without and **b** with 0.5% bentonite

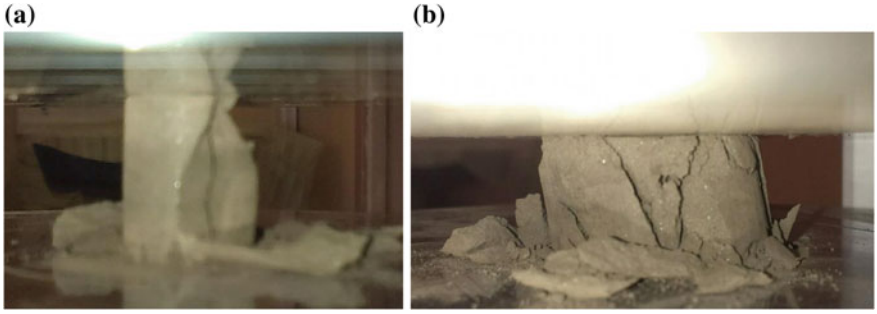

Fig. 2.11 Fracture of brex based on aspiration dust: compositions **a** without and **b** with 0.5% bentonite. The initial brex sizes are 50 mm in height and 25 mm in diameter

ultimate compressive strength of the brex made of a bentonite-free mixture is 1.88 MPa and that of bentonite-containing brex is 2.08 MPa (higher by 10%).

As for traditional methods of briquetting, the favorable effects of bentonite or bentonite in combination with Portland cement on the strength of briquettes is well known [12, 13]. An attempt to determine the optimum ratio of the fractions of Portland cement and bentonite in a charge to be briquetted was described in patent [14]. It was stated that the addition of a bentonite (15–25%) and Portland cement (85–75%) binder enhances the mechanical strength of the corresponding briquette. For briquettes consisting of converter sludge (24.3%), scale (23.4%), blast furnace dust (23.4%), iron ore fines (18.9%), and binder (10%) consisting of 75% Portland cement and 25% bentonite, the result of a drum test (fraction of a size of >6.3 mm)

increased to 76% (it was 67% for briquettes of the same composition but without bentonite).

We studied the influence of this combined binder on both the compressive strength of brex and the rate of strength augmentation during strengthening storage under natural conditions. For tests, we chose the brex that were produced in the industrial line of stiff vacuum extrusion located at Suraj Products Ltd. (India) and contained (%) 47.2 converter sludge, 28.3 blast furnace dust, 18.9 iron ore fines, 4.7 Portland cement, and 0.9 bentonite. Portland cement and bentonite were manually mixed in a dried state and added to a charge mixture before a pug sealer. For brex samples, we measured compressive strength σ (on Tonipact 3000 (Germany) according to standard DIN 51067), open (apparent) porosity η (vacuum method of liquid saturation according to standard DIN 51056), and density ρ (on Metler (United States) balance) daily. Table 2.3 shows the results of our daily measurements over the course of 9 days.

Figure 2.12 shows the brex porosity and strength curves measured during structuring storage. A pronounced local maximum is clearly visible in the brex strength curve on the third day. On the next day, this changes into softening. The strength increases over the course of further storage. Note that, before softening, the brex strength accounts for $\sim$84% of the brex strength after strengthening storage for 1 week. The change of open porosity almost repeats the change of strength, except for the first day of strengthening. The decrease in the porosity at that time is obviously related to the swelling of bentonite, which fills the pore space [15].

We obtained similar results for brex strength during compressive strength and splitting strength tests performed on a strength-testing machine consisting of a hand-power press, a strain gage, and a recording device (Fig. 2.13).

On the third day of strengthening, the brex samples retained their integrity through the end of testing and demonstrated a viscoplastic character of fracture during compressive and tensile splitting tests. On the third day of strengthening, both halves of the brex were connected despite the development of almost a

Table 2.3 Results of the daily measurements of the brex apparent porosity, density, and compressive strength

Maturing time, days	Apparent porosity %	Density (g/cm^3)	Compressive strength (kg/cm^2)
1	31.5	2.42	24
2	25.4	2.66	45
3	32	2.43	63
4	27	2.44	52
5	27.2	2.45	56
6	26.2	2.45	57
7	26.8	2.46	59
8			75
9			80

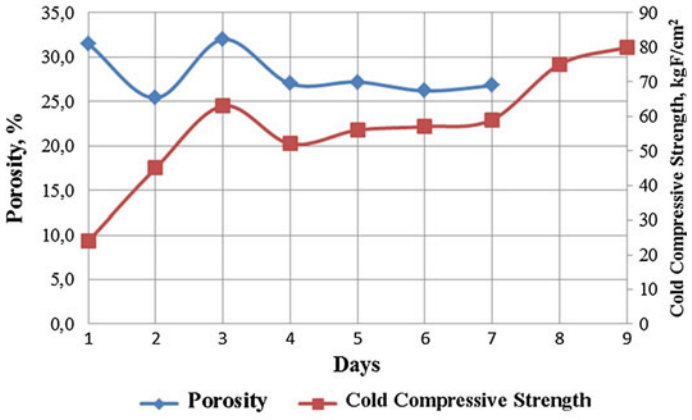

Fig. 2.12 Changes in compressive strength and porosity of brex during strengthening 9-day storage

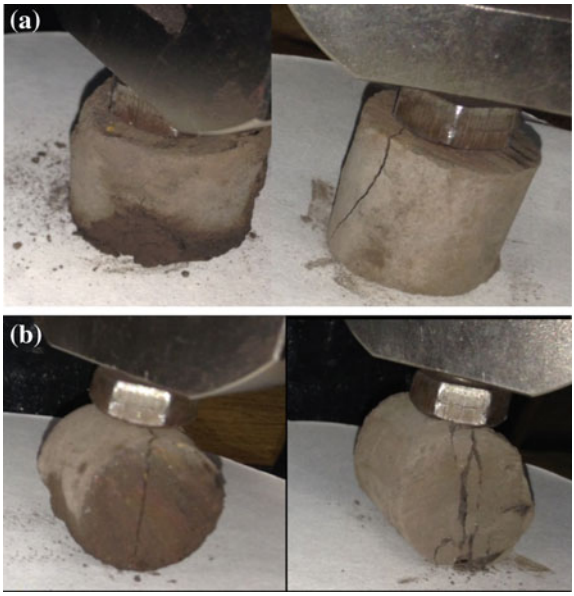

Fig. 2.13 **a** Axial compression and **b** tensile splitting tests of the brex produced at Suraj Products Ltd. at the third (**a**, **b** on the left) and seventh (on the right) day of strengthening storage. The initial brex sizes are 25 mm in height and 25 mm in diameter

complete crack in the tensile splitting test. The compression and splitting of brex led to the release of moisture on the bottom. Moisture release was absent during compression on the seventh day of strengthening. When samples were subjected to compressive and tensile splitting tests on the seventh day of strengthening, the viscoplastic character of fracture was substantially lost.

This effect of nonmonotonic strengthening of briquettes with a cement binder, characterized by a local strength maximum and accompanied by viscoplastic

behavior at a breaking load, had been neither detected nor described previously. The strengthening of monomineral cement stone and concrete is known to be of a monotonic character [16]. This nonmonotonic character is well noted in the process of increasing the strength of binderless brex or of brex with an alternative (no cement) binder. Ozhogin [17] presents data on the impact fracture (analog of dropping strength) oscillations of briquettes having no binder and having different compositions upon drying under natural conditions (at a temperature of 20 °C). The detected softening was thought to be caused by recrystallization, and it was recommended to limit the transportation and transfer of briquettes at this time and to store briquettes in closed vessels.

The application of a cement–bentonite binder changes the behavior of brex substantially during a braking action, increases its impact strength, and decreases the probability of brittle fracture.

This behavior of brex can be explained by cement–bentonite binder properties related to the formation of coagulation structures in the cement–bentonite–water system, which leads to the modification of the properties of the binder. Such structures are known to form in the gel–cement solutions used for the cementation of boreholes. The properties of the gel–cement solutions and the theoretical and practical aspects of the formation and fracture of cement–bentonite systems are well known and systematized in, e.g., [18]. The driving force of the formation of such structures is the attraction of negatively charged bentonite particles to positively charged Portland cement particles, which results in their rapid coagulation and the formation of a suspended cement particle structure. Hydrated cement particles are gradually coated with an impermeable shell of flaky bentonite particles. The number of adsorbed bentonite particles is proportional to the activity of cement. During hydration, Portland cement particles grow in size, which leads to tension, a break in the integrity of bentonite shells, and the penetration of water to cement particles (i.e., to further hydration of cement and, apparently, the adsorption of a larger amount of bentonite).

The fracture intensity of such a coagulation structure depends on the cement activity. The application of slag Portland cement is likely to retard this process. The coagulation structure begins to fail gradually as a result of the coagulation effect of calcium ions and changes into the structure of a hardening cement stone. The decrease in the strength after the peak at the third day is explained by the decomposition of the coagulation structure (Fig. 2.12). The further increase in strength is completely determined by the hydration of cement stone.

The possibility of such a stable structure forming is supported by the conclusions of work [19]. The range of the relative content of bentonite and Portland cement in the binder used for the production of brex (80% Portland cement, 20% bentonite) corresponds to the dark gray region in the water–cement–bentonite phase diagram (Fig. 2.14 [19]).

Note that the local moisture content near coagulated particles exceeds the moisture content of the as-prepared brex substantially (by 11–12%) due to differences in the permeability of minerals. An increase in the fraction of bentonite in the binder up to 30–40% favors the formation of a stable mastic suspension.

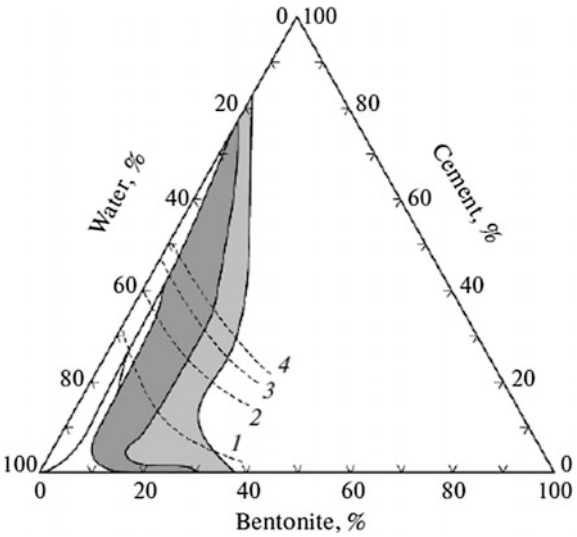

Fig. 2.14 Water–cement–bentonite phase diagram [19]. (Light gray) region of formation of a stable mastic suspension and (dark gray) region of a stable and mobile suspension. (1–4) compressive strength values, kPa: (1) 69, (2) 345, (3) 689, and (4) 1378

The effect revealed in this work can be important for practice: brex based on a cement–bentonite binder can be used as a charge component for a metallurgical furnace within 3 days of drying under natural conditions. As a result, the required sizes of brex storage can be decreased. The threshold level of compressive strength can be easily achieved by a simple increase in the fraction of this combined binder. Note that the total fraction of a binder in the brex produced at Suraj Products Ltd. accounts for at most 5.6% of the brex mass, which is significantly lower than the required content of Portland cement used for vibropressing briquetting (10–12%). The use of bentonite in the binder composition changes the character of fracture of briquettes and makes it viscoplastic, which simplifies the transportation of brex to the site of its application. A quantitative description of the detected effect is the subject of further investigation.

The moisture release during the briquette strength tests on the third day can be related to restructuring in the agglomerates formed in cement during its hydration, which is accompanied by the release of part of chemically fixed water. It is known that, at a sufficiently high content of volume capillary moisture in cement, intense nucleation and growth of acicular aggregates take place on the third day of hardening [20]. It is these aggregates that are responsible for the connection of cement grains and prevent crack development in primary aggregates, and these aggregates were experimentally detected in the cleavages of commercial brex. The experimental investigation was carried out using a high-resolution scanning electron microscopy (SEM) on an Auriga CrossBeam (Carl Zeiss) analytical working station equipped with an INCA X-Max energy dispersive spectrometer. The accelerating voltage was 20 kV. During the hydration of cement, ettringite forms as a result of the reaction between calcium aluminate and sulfate: $3CaO \cdot Al_2O_3 + 3CaSO_4 \rightarrow$ Ettringite.

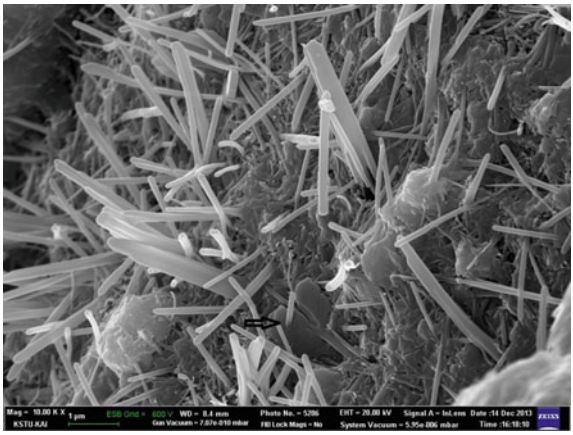

Fig. 2.15 SEM micrograph of acicular aggregates (ettringite particles) surrounded by bentonite plates in cement in the structure of the brex produced at Suraj Products Ltd.

Using SEM, we were able to reveal the elements of the decomposed coagulation structure. Ettringite particles surrounded by bentonite plates are visible in Fig. 2.15.

The change in the properties of brex induced by the addition of bentonite to the composition of the mixture to be briquetted also manifests itself after the preliminary homogenization of the mixture to be briquetted during its "souring" (storage of the moisturized mixture with added bentonite for within a certain time). This method allows achieving a high degree of homogeneity of mixture properties for subsequent briquetting. In some cases, the mechanical strength of brex made of homogenized charge can significantly increase. Consumption of plasticizer for briquetting the charge without prior homogenization, in this case, can decrease significantly. We studied the effect of souring on the strength of brex of various compositions (Table 2.4). Table 2.5 gives the results of tensile splitting tests of brex 1 week after its manufacture. These results demonstrate that the use of bentonite in combination with Portland cement improves the strength properties of brex. The strength of brex increases substantially in some cases. Furthermore, the manner of their fracture also changes and signs of viscoplastic fracture appear. In this case, brex can better withstand the impact loads that appear during their transportation to the sites of their application.

Table 2.4 Brex compositions for testing of the souring efficiency

Brex composition/No.	1	2	3	4	5	6
BF sludge	42.8	41.8	41.8	41.2	47.8	28.3
BOF sludge	39.8	38.8	38.8	38.2	43.7	25.4
Iron ore concentrate						29.3
Mill scale	13.0	13.0	13.0	12.1		10.7
Portland cement	4.0	4.0	6.0	8.0	8.0	5.8
Bentonite	0.4	0.4	0.4	0.5	0.5	0.5
Microsilica		2.0				

Table 2.5 Values of tensile splitting strength of brex

Tensile splitting strength of brex, MPa	1	2	3	4	5	6
Without souring	0.86	1.93	2.08	1.00	1.01	0.77
After souring	2.45	3.83	5.76	1.88	1.29	1.26
The ratio of strength values	2.85	1.98	2.76	1.88	1.28	1.64

Table 2.6 Granulometric composition of brex components

Material	Fraction, mm/yield, mass%					
	−20… + 10	−10… + 5	−5… + 2	−2… + 1	−1… + 0.5	−0.5
Manganese ore concentrate, %	3.42	25.42	32.58	18.95	9.70	9.93
Baghouse dust of SiMn production	Fine dust, size less than 0.063 mm					

The results of the study on the effects of shearing stress on the properties of extruded mixture allow using shearing through the shearing plate for the homogenization of the mixture prior to its agglomeration with binder.

To demonstrate the effect of such operations on the homogenization of the mixture, we have compared values of compressive strength on brex composed of manganese ore concentrate with added baghouse dust resulting from silicomanganese production with and without homogenizing the earlier-sheared mixture.

The granulometric composition of brex components is listed in Table 2.6. The composition of brex is given in Table 2.7.

A laboratory extruder has been used for brex sample production. The sheared mix was subjected to the souring over the course of 4 h. Table 2.8 shows the results of the measurement of the compressive strengths of brex No. 1–3 produced from this mix with and without souring. The increase in compressive strength a week after manufacturing was 14.2% for brex No. 1; 7.62% for brex No. 2, and 54.5% for brex No. 3.

Study of the brex structure by means of scanning electronic microscopy revealed differences in the structure and distribution of pores. Figure 2.16 presents the structure of the brex No. 2.

One can see that pore size is significantly smaller in the brex made from a sheared and soured mix. Our results confirm the efficiency of using a shearing extruder in preparing the briquette charge for souring.

Table 2.7 Composition of brex

Composition of brex	No. 1	No. 2	No. 3
Manganese ore concentrate	80	66	56
Baghouse dust	14	28	38
Portland cement	5	5	5
Bentonite	1	1	1

Table 2.8 Compressive strength of brex No. 1–3

Strength/ brex No	No. 1	No. 1— soured	No. 2	No. 2— soured	No. 3	No. 3— soured
Day 1 (MPa)	2.9647	2.7579	2.6890	5.7571	4.0955	6.1708
Day 3 (MPa)	4.8608	4.8608	6.0674	7.8255	6.1019	10.2042
Day 7 (MPa)	6.6741	7.6187	13.1345	14.3411	10.1698	15.7200

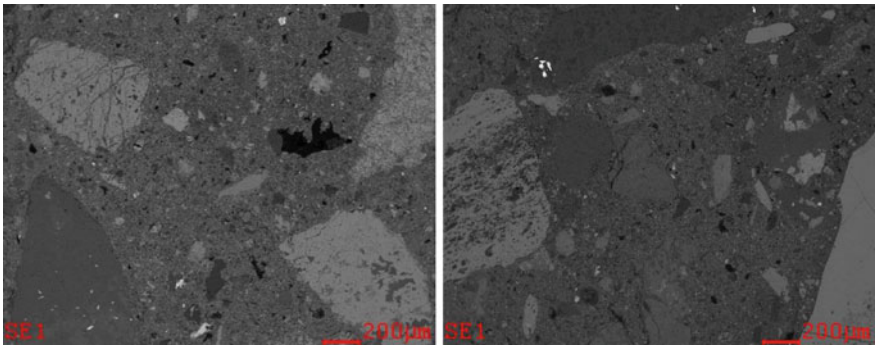

Fig. 2.16 Scanning electron microscopy of the brex No. 2 structure. Left—without souring; right—with souring during 4 h after shearing

2.2 Technological Process of Briquetting by Method of Stiff Vacuum Extrusion

Typical layouts of the SVE briquetting line is shown in Fig. 2.17.

Prepared in the warehouse of the raw material mixture of the main components of the brex mix is being fed by an even feeder (Fig. 2.18), equipped with spirals cast of chrome alloy.

Next, the prepared mixture with added binder and plasticizer is fed for mixing in the pug sealer. The line can also contain primary open pug-mill. The pug sealer consists of a large open part and the sealing node. The open part (Fig. 2.19) consists of a trough and system blades for mixing. The blades are fastened to the steel rod shaft by bolted clamps, making it possible to rotate the blades to adjust the angle at which the processing takes place and, thereby, change the machine's performance.

The pug sealer is combined in a single unit with the extruder and is positioned above it (Fig. 2.20).

The mixture enters the vacuum chamber partially agglomerated (Fig. 2.21) and due to the high vacuum inside the chamber and removal of air and moisture, the pieces of the mixture immediately crumble into isolated particles, which fall down on the blades of the auger. It is known [21] that the air adsorbed by the surface of the particles of plastic material in the form of multi-molecular layers held by van der Waals forces slow the rate at which they wetten, prevents the mass's uniform

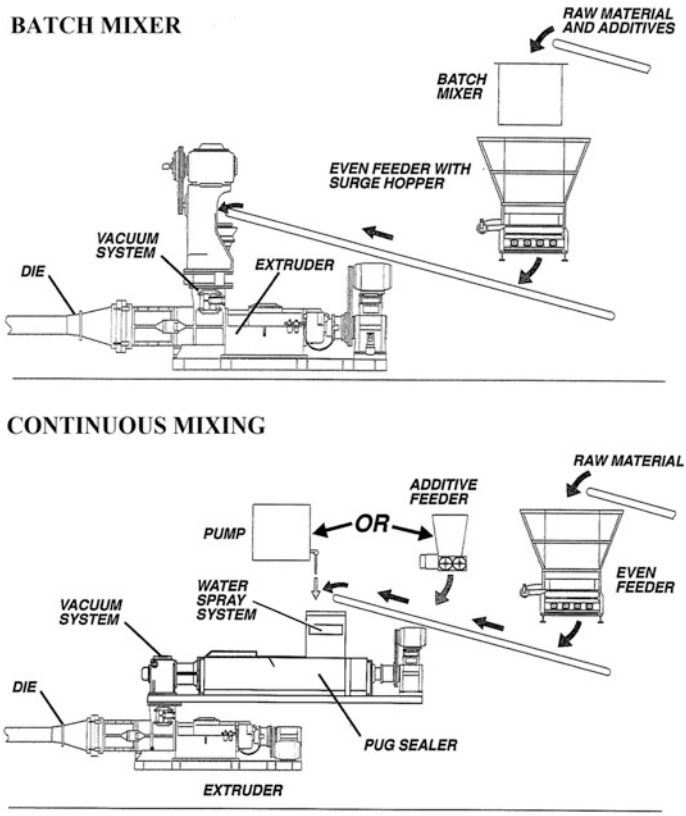

Fig. 2.17 Typical layouts of SVE briquetting line

Fig. 2.18 J.C. Steele E Series Even Feeder

Fig. 2.19 Mixing in the open part of the pug sealer

Fig. 2.20 The appearance of extruder (bottom) and pug sealer

Fig. 2.21 Partial agglomeration of the mix in pug sealer

compaction, and promotes elastic deformation, which results in lamination and micro-cracks detected during the drying and firing of products. In filling the pores, the air also prevents moisture from penetrating, separates the particles of the mass, and acts as a leaner. The vacuum removes air from the pores and promotes the closer contact of particles.

The vacuum is maintained throughout the working volume of the extruder up to the die. The pressure of the vacuum is at least 100 mm Hg (in absolute value). The area of the vacuum in the working chamber of the extruder and pug sealer is shown in Fig. 2.22. The combination of mechanical pressure and vacuum in the working extruder chamber helps to remove almost all compressible air from the material before densifying, which leads the green brex to have high values of compressive strength of and to immediately be transported by conveyors and stockpiled, practically without fines. In addition, as is well known, the vacuum slightly decreases the viscosity of the cement paste, which facilitates its uniform distribution in the briquetting mass and improves its interaction with water [22]. This, combined with a higher density of mass resulting from the removal of air, leads to a decrease in cement binder consumption.

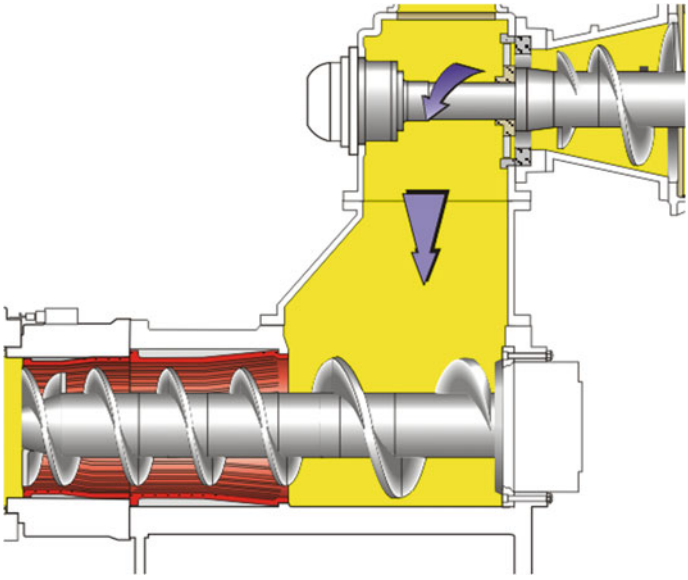

Fig. 2.22 Vacuum area in extruder and pug sealer

2.3 The Movement of the Briquetted Mass in the Extruder

Due to rotation of the auger blades in the working chamber of the extruder, formable mass performs translational and rotational motion, which is slowed by the walls (Fig. 2.23).

In the conveying zone, the material is loose and moves along the barrel without densification. Bulk density remains unchanged. Zone 2 is the densifying region where the loose material is compacted. In zone 3, metering is achieved by way of the special geometry of the wings of the point auger. Zone 4 serves the purpose of distributing the pressure generated by the metering zone more evenly over the die, thus tending to yield a more even flow through it.

Bizhanov et al. made a preliminary assessment of the briquetted mass movement in the working chamber of the extruder from the point of view of basic continuum mechanics [23]. The rotating mass of a wet, continuous medium has an isotropic molecular pressure field [2, 24] and is subject to the fundamental laws of conservation of mass, momentum, and energy [25–27] with an appropriate rheology for the coefficient of dynamic viscosity μ [28–30].

First of all, as in [31], the motion of a particle, or point $\mathbf{r} = x\mathbf{i} + y\mathbf{j} + z\mathbf{k}$, will be measured in cylindrical coordinates r, θ, z,

$$r = \left(x^2 + y^2\right)^{1/2}], \text{ and } \theta = \text{acrtg}\frac{y}{x}, \text{ or } x = r\cos\theta \text{ and } y = r\sin\theta,$$

or in polar orts

$$\mathbf{I} = \mathbf{cos}\,\theta = \mathbf{i}\cos\theta + \mathbf{j}\sin\theta \text{ and } \mathbf{J} = -\mathbf{sin}\,\theta = \mathbf{j}\cos\theta - \mathbf{i}\sin\theta \text{ and } \mathbf{k}$$

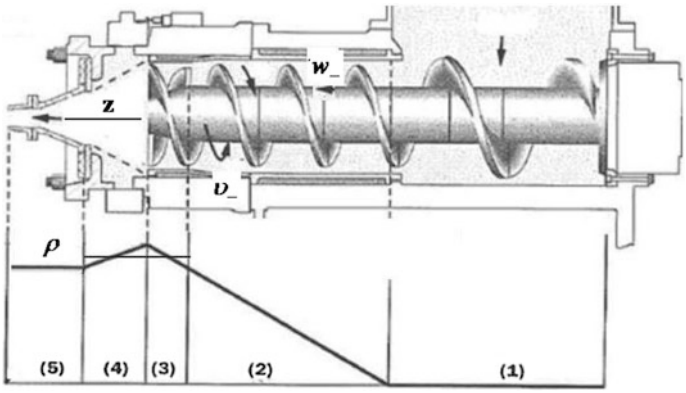

Fig. 2.23 Stages of densifying in the working zone of the extruder. 1—conveying, 2—densifying, 3—metering, 4—pressure distributing, 5—die

preserving the sum of the double orts of the direct product and

$$\mathbf{ii} + \mathbf{jj} = \mathbf{II} = \mathbf{JJ},$$

"inheriting" the properties of the sine and cosine functions,

$$\mathbf{I}_\theta = \partial_\theta \mathbf{I} = \frac{\partial \mathbf{cos}\,\theta}{\partial \theta} = -\mathbf{sin}\,\theta = \mathbf{J} \text{ and } \mathbf{J}_\theta = -\partial_\theta \mathbf{sin}\,\theta = -\mathbf{cos}\,\theta = -\mathbf{I},$$

but otherwise remaining the same as the Cartesian orts $\mathbf{i}, \mathbf{j}, \mathbf{k}$:

$$\mathbf{I} \times \mathbf{J} = \mathbf{i} \times \mathbf{j} = \mathbf{k},\ \mathbf{J} \times \mathbf{k} = \mathbf{I},\ \mathbf{k} \times \mathbf{I} = \mathbf{J},$$
$$\mathbf{I} \cdot \mathbf{J} = \mathbf{J} \cdot \mathbf{k} = \mathbf{k} \cdot \mathbf{I} = 0 \text{ and } \mathbf{I} \cdot \mathbf{I} = \mathbf{J} \cdot \mathbf{J} = \mathbf{k} \cdot \mathbf{I} = 1,$$

so:

$$\mathbf{r} = x\mathbf{i} + y\mathbf{j} + z\mathbf{k} = r\mathbf{I}(\theta) + z\mathbf{k}.$$

In addition the specified field mass accelerations,

$$\mathbf{g}(t, \mathbf{r}) = g^x \mathbf{i} + g^y \mathbf{j} + g^z \mathbf{k} = g^r \mathbf{I} + g^\theta \mathbf{J} + g^z \mathbf{k},$$

field velocities or flow

$$\mathbf{u}(t, \mathbf{r}) = u^x \mathbf{i} + u^y \mathbf{j} + u^z \mathbf{k} = u\mathbf{I} + \upsilon \mathbf{J} + w\mathbf{k} = \mathbf{r}_t,$$

receives three components of velocity, axial $w = z_t$, radial, $u = r_t$, and azimuthal, $\upsilon = r\theta_t$ from the polar orts

$$u^z = w, u^x = u\,\cos\theta - \upsilon\,\sin\theta,\ u^z = u\,\sin\theta + \upsilon\,\cos\theta,$$

will be considered further to be axially symmetric, or independent of the polar angle θ:

$$u_\theta = \upsilon_\theta = w_\theta = \rho_\theta = p_\theta = g^r_\theta = g^z_\theta = 0 \text{ for } g^\theta = 0.$$

In this case, the gradient

$$\nabla = \begin{pmatrix} \mathbf{i}\partial_x \\ +\mathbf{j}\partial_y \\ +\mathbf{k}\partial_z \end{pmatrix} = \begin{pmatrix} \mathbf{I}\partial_r + \mathbf{k}\partial_z \\ +\mathbf{J}\dfrac{\partial_\theta}{r} \end{pmatrix}, \partial_x = \cos\theta\partial_r - \frac{\sin\theta}{r}\partial_\theta, \partial_y$$
$$= \sin\theta\partial_r + \frac{\cos\theta}{r}\partial_\theta,$$

and divergences

$$\nabla\cdot\ \rho\mathbf{u}=\begin{pmatrix}\mathbf{I}\partial_r+\mathbf{k}\partial_z\\ +\mathbf{J}\dfrac{\partial_\theta}{r}\end{pmatrix}\cdot\begin{pmatrix}\mathbf{I}\rho\upsilon\\ \mathbf{J}\rho\upsilon\\ +\mathbf{k}\rho w\end{pmatrix}=\begin{pmatrix}(\rho u)_r\\ +(\rho w)_z\end{pmatrix}+\frac{1}{r}\mathbf{J}\cdot\begin{pmatrix}\rho u\mathbf{I}_\theta\\ +\rho\upsilon\mathbf{J}_\theta\end{pmatrix},\mathbf{I}_\theta$$
$$=\mathbf{J},\mathbf{J}_\theta=-\mathbf{I},$$

and

$$\nabla\cdot\ \mu\nabla u=\begin{pmatrix}\mathbf{I}\partial_r+\mathbf{k}\partial_z\\ +\mathbf{J}\dfrac{\partial_\theta}{r}\end{pmatrix}\cdot\begin{pmatrix}\mathbf{I}\mu u_r\\ +\mathbf{k}\mu u_r\end{pmatrix}=\begin{pmatrix}(\mu u_r)_r\\ +(\mu u_z)_z\end{pmatrix}+\frac{1}{r}\mathbf{J}\cdot\mathbf{I}\mu u_r,\ldots,$$

lead to the following mass, momentum, and viscous volumetric densities:

$$\nabla\cdot\rho\mathbf{u}=\frac{1}{r}(r\rho u)_r+(\rho w)_z,\nabla\cdot\rho u\mathbf{u}=\frac{1}{r}(r\rho uu)_r+(\rho uw)_z$$
$$\text{and }\nabla\cdot\mu\nabla u=\frac{1}{r}(r\mu u)_r+(\mu u_z)_z,\ldots\text{for }\mu=\mu(t,\mathbf{r}),$$

respectively.

Furthermore, in order to save records, as in [32], let us represent the matrices by double vectors, or more specifically by divectors: an identity matrix is the sum of the direct squares of the orts

$$\vec{\mathbf{e}}=\begin{pmatrix}1&0&0\\0&1&0\\0&0&1\end{pmatrix}=\mathbf{ii}+\mathbf{jj}+\mathbf{kk}=\mathbf{II}+\mathbf{JJ}+\mathbf{kk},$$

further, the matrix of momentum flow by the proportion $\rho\mathbf{uu}$ of $\mathbf{uu}=(u\mathbf{I}+\upsilon\mathbf{J}+w\mathbf{k})\mathbf{u}$ density of momentum flow

$$\nabla\cdot\rho\mathbf{uu}=\left(\nabla\cdot\rho u\mathbf{u}-\frac{\rho\upsilon^2}{r}\right)\mathbf{I}+\left(\nabla\cdot\rho u\mathbf{u}+\frac{\rho\upsilon u}{r}\right)\mathbf{J}+(\nabla\cdot\rho w\mathbf{u})\mathbf{k},$$

finally, the original for fluid mechanics the "matrix of the deformation rates" [33] by the matrix of the rate deformations, or fluid deformations $\mathbf{u_r}$ to be the sum of $\mathbf{u}_x\mathbf{i}+..$ of direct products $\mathbf{u}_x\mathbf{i}+..$:

$$\mathbf{u_r}=\begin{pmatrix}u_x^x&u_y^x&u_z^x\\u_x^y&u_y^y&u_z^y\\u_x^z&u_y^z&u_z^z\end{pmatrix}=\begin{pmatrix}u_x^x\mathbf{ii}+&u_y^x\mathbf{ij}+&u_z^x\mathbf{ik}+\\u_x^y\mathbf{ji}+&u_y^y\mathbf{jj}+&u_z^y\mathbf{jk}+\\u_x^z\mathbf{ki}+&u_y^z\mathbf{kj}+&u_z^z\mathbf{kk}\end{pmatrix}=\mathbf{u}_x\mathbf{i}+\mathbf{u}_y\mathbf{j}+\mathbf{u}_z\mathbf{k},$$

or

$$\mathbf{u_r} = \mathbf{u}_r\mathbf{I} + \frac{1}{r}\mathbf{u}_\theta\mathbf{J} + \mathbf{u}_z\mathbf{k},$$

with

$$\mathbf{u}_\theta = (u\mathbf{I} + \upsilon\mathbf{J} + w\mathbf{k})_\theta = u\mathbf{I}_\theta + \upsilon\mathbf{J}_\theta = u\mathbf{J} - \upsilon\mathbf{J} = \mathbf{k}\times\mathbf{u}$$
$$\text{and } \mathbf{u}_{\theta\theta} = \mathbf{k}\times\mathbf{k}_\theta = \mathbf{k}\times(\mathbf{k}\times\mathbf{k}) = \mathbf{k}\mathbf{k}\cdot\mathbf{u} - \mathbf{k}\cdot\mathbf{k}\mathbf{u} = \mathbf{k}w - \mathbf{u},$$

with divergence

$$\nabla\cdot\mathbf{u}_r = \left(\frac{1}{r}(ru)_r + w_z\right)_r\mathbf{I} + \left(\frac{1}{r}(ru)_r + w_z\right)_z\mathbf{k} = (\nabla\cdot\mathbf{u})_r\mathbf{I} + (\nabla\cdot\mathbf{u})_z k = \nabla\nabla\cdot\mathbf{u}$$

convolution or point product

$$\nabla\mu\cdot\mathbf{u}_r = (\nabla\mu\cdot\mathbf{u}_r)\mathbf{I} - \frac{\mu_r\upsilon}{r}\mathbf{J} + (\nabla\mu\cdot\mathbf{u}_z)\mathbf{k},$$

with divergence

$$\begin{aligned}\nabla\cdot\mu\mathbf{u_r} &= \mu\nabla\cdot\mathbf{u_r} + \nabla\mu\cdot\mathbf{u_r} = \mu\nabla\nabla\cdot\mathbf{u} + \nabla\mu\cdot\mathbf{u_r}\\ &= \big(\mu(\nabla\cdot\mathbf{u})_r + \nabla\mu\cdot\mathbf{u}_r\big)\mathbf{I} - \frac{\mu_r\upsilon}{r}\mathbf{J} + \big(\mu(\nabla\cdot\mathbf{u})_z + \nabla\mu\cdot\mathbf{u}_z\big)\mathbf{k},\end{aligned}$$

and the conjugate matrix is the sum of the corresponding reverse multiplications

$$\nabla\mathbf{u} = \begin{pmatrix} u_x^x & u_x^y & u_x^z \\ u_y^x & u_y^y & u_y^z \\ u_z^x & u_z^y & u_z^z \end{pmatrix} = (\nabla\mu^x)\mathbf{i} + (\nabla\mu^y)\mathbf{j} + (\nabla\mu^z)\mathbf{k} = \mathbf{i}\mathbf{u}_x + \mathbf{j}\mathbf{u}_y + \mathbf{k}\mathbf{u}_z,$$

or

$$\nabla\mathbf{u} = (\mathbf{u_r})_* = \mathbf{I}\mathbf{u}_r + \frac{1}{r}\mathbf{J}\mathbf{u}_\theta + \mathbf{k}\mathbf{u}_z, \cdots \mathbf{u_r} = (\nabla\mathbf{u})_*,$$

with divergence

$$\nabla\cdot\mu\nabla\mathbf{u} = \left(\nabla\cdot\mu\nabla u - \frac{\mu u}{r^2}\right)\mathbf{I} + \left(\nabla\cdot\mu\nabla\upsilon - \frac{\mu u}{r^2}\right)\mathbf{J} + (\nabla\cdot\mu\nabla w)\mathbf{k}$$

so that

$$\nabla\cdot\mu(\mathbf{u}_r + \nabla\mathbf{u}) = \begin{pmatrix} \nabla\cdot\mu\nabla u - \frac{\mu u}{r^2} \\ +\mu(\nabla\cdot\mathbf{u})_r + \nabla\mu\cdot\mathbf{u}_r \end{pmatrix}\mathbf{I} + \begin{pmatrix} \nabla\cdot\mu\nabla\upsilon \\ -\frac{(r\mu)_r\upsilon}{r^2} \end{pmatrix}\mathbf{J} + \begin{pmatrix} \nabla\cdot\mu\nabla w \\ +\mu(\nabla\cdot\mathbf{u})_z \\ +\nabla\mu\cdot\mathbf{u}_z \end{pmatrix}\mathbf{k}.$$

Let us consider the motion of the particles in the wet mixture. If we follow Euler and add the strength of the molecular pressure p to Newton's law of dynamics, then, taking into account conservation of mass or the continuity equation

$$\rho_t + \nabla \cdot \rho\mathbf{u} = 0$$

add the buoyant force of Archimedes $-\nabla p$ (or the force of molecular pressure p) to the body force (or, to be exact, $\mathbf{g}\rho \mathrm{d}V$) applied to mass $\rho \mathrm{d}V$ with a given acceleration $\mathbf{g} = \mathbf{g}(t, \mathbf{r})$ in the Newton's dynamic law that balances the inertial force $\rho\mathbf{a}$ of fluid acceleration $\mathbf{a} = \mathbf{u}_t + \mathbf{u} \cdot \nabla\mathbf{u}$ with the sum of $\rho\mathbf{g}$ and $-\nabla p$ refined subsequently by both the force $\nabla \cdot \mu\vec{\mathbf{b}}$ of the Newton's dynamic viscosity $\mu = \mu(t, \mathbf{r})$ (supposed to be constant initially) and the matrix

$$\vec{\mathbf{b}} = \mathbf{u}_\mathbf{r} + \nabla\mathbf{u} - \frac{2}{3}(\nabla \cdot \mathbf{u})\vec{\mathbf{e}},$$

of Navier ($\nabla \cdot \mathbf{u} = 0$) and Stokes and the relevant pressure force $-\nabla(p - \varsigma\mu\nabla \cdot \mathbf{u})$ with the second, or volume viscosity $\varsigma\mu$, $\varsigma = \mathrm{cons} \geq 0$ [26–28].

As a result, with appropriate contact (or applied to coordinate areas) forces to be tensions, stresses, or components of the Euler–Navier–Stokes matrix

$$\vec{\mathbf{p}} = (p - \varsigma\mu\nabla \cdot \mathbf{u})\vec{\mathbf{e}} - \mu\vec{\mathbf{b}} = P\vec{\mathbf{e}} - \mu(\mathbf{u}_r + \nabla\mathbf{u}),\ P = p + \left(\frac{2}{3} - \varsigma\right)\mu\nabla \cdot \mathbf{u},$$

with divergence

$$\nabla \cdot \vec{\mathbf{p}} = \nabla \cdot P\vec{\mathbf{e}} - \nabla \cdot \mu(\mathbf{u}_r + \nabla\mathbf{u}) = \nabla P - \nabla \cdot \mu(\mathbf{u}_r + \nabla\mathbf{u}),$$

and ensures the dynamic equilibrium of a continuous medium in the corresponding Navier–Stokes equations:

$$(\rho\mathbf{u})_t + \nabla \cdot (\rho\mathbf{u}\mathbf{u} + \vec{\mathbf{p}}) = \rho\mathbf{g} \text{ and } \rho_t + \nabla \cdot \rho\mathbf{u} = 0, \tag{2.1}$$

or

$$\begin{gathered}
(\rho u)_t + \left(\tfrac{1}{r}(r\rho uu)_r + (\rho uw)_z - \tfrac{\rho v^2}{r}\right) + P_r \\
-\left(\tfrac{1}{r}(r\mu u_r)_r + (\mu u_z)_z - \tfrac{\mu u}{r^2} + \mu\left(\tfrac{1}{r}(r\mu)_r + (w)_z\right)_r + \mu_r u_r + \mu_z w_r\right) = \rho g^r, \\
(\rho v)_t + \left(\tfrac{1}{r}(r\rho vu)_r + (\rho vw)_z + \tfrac{\rho uv}{r}\right) - \left(\tfrac{1}{r}(r\mu v_r)_r + (\mu v_z)_z - \tfrac{(r\mu)_r v}{r^2}\right) = 0, \\
(\rho w)_t + \left(\tfrac{1}{r}(r\rho wu)_r + (\rho ww)_z\right) + P_z \\
-\left(\tfrac{1}{r}(r\mu w_r)_r + (\mu w_z)_z + \mu\left(\tfrac{1}{r}(ru)_r + w_z\right)_z + \mu_r u_z + \mu_z w_z\right) = \rho g^z, \\
P = p + \mu\left(\tfrac{2}{3} - \varsigma\right)\left(\tfrac{1}{r}(ru)_r + w_z\right) \text{and } \rho_t + \tfrac{1}{r}(r\rho u)_r + (\rho w)_z = 0,
\end{gathered}$$

Contact stresses of matrix $\mathbf{P}$ are naturally attributed to the source of liquid strains $\mathbf{u}_\mathbf{r}$ for particles of the wet mixture in dynamic equilibrium (Eq. 2.1), which replaces

static equilibrium (Hooke's law) for small displacements in the solid particles of the dry material [33].

The distortion of the velocity field assessed using measurement of liquid deformation [32],

$$D = D[\mathbf{u}] = \frac{1}{2}\|\mathbf{u_r} + \nabla\mathbf{u}\|^2 = \frac{1}{2}|\mathbf{u}_x + \nabla u^x|^2 + \frac{1}{2}|\mathbf{u}_y + \nabla u^y|^2 + \frac{1}{2}|\mathbf{u}_z + \nabla u^z|^2, \ldots$$

which is a familiar function measuring the dissipation of mechanical energy into thermal energy [27],

$$D = 2\left(u_x^x\right)^2 + 2\left(u_y^y\right)^2 + 2\left(u_z^z\right)^2 + \left(u_x^y + u_y^x\right)^2 + \left(u_y^z + u_z^y\right)^2 + \left(u_z^x + u_x^z\right)^2$$

or, in the axisymmetric polar variables

$$D = 2u_r^2 + 2\left(\frac{u}{r}\right)^2 + 2w_z^2 + \left(v^r - \frac{v}{r}\right)^2 + (v_z)^2 + (u_z + w_r)^2,$$

and systematically used, as shown, for example, in [34], the argument (or independent variable) of viscous rheology, suggesting the existence of an equation to measure the plastic state of the material [28–30]:

$$\mu = \mu(\gamma),\ \gamma = D[\mathbf{u}] \geq 0.$$

The geometric structure of the argument $\gamma = D$ reveals the identity of measure, as directly verifiable resolving D the sum of the proportions [32],

$$D = \frac{2}{3}A^2 + B^2 + \frac{2}{3}C^2$$

squares of local norms of inhomogeneity

$$A = \sqrt{\left(u_x^x - u_y^y\right)^2 + \left(u_y^y - u_z^z\right)^2 + \left(u_z^z - u_x^x\right)^2},$$

shear

$$B = \sqrt{\left(u_x^y - u_y^x\right)^2 + \left(u_y^z - u_z^y\right)^2 + \left(u_z^x - u_x^z\right)^2},$$

and compressibility

$$C = u_x^x + u_y^y + u_z^z$$

for liquid deformations, described by the matrix $\mathbf{u_r}$.

It is possible to show [15] that with the help of proper deformations of inhomogeneity, shear, and compressibility, material mixed in the arbitrary volume V, produces work in a second, or power of deformations

$$W = \int_V \mu\left(\frac{2}{3}A^2 + B^2 + \varsigma C^2\right)\mathrm{d}V.$$

Let us simplify the initial problem. As already noted, in addition to transportation, the main purpose of the extruder is to compact the material in zone 2 (Fig. 2.20). We will limit ourselves to the portion (length) of zones 3 and 4, suggesting constant density of material, approximated by Newtonian rheology:

$$\rho = \mathrm{const} > 0\,(\text{therefore, } \nabla \cdot \mathbf{u} = 0)\,\text{and}\,\mu = \mathrm{const} > 0.$$

We consider the flow of material in the space between two concentric infinite cylinders. Further, with the stationary external cylinder $r = a = \mathrm{const} > 0$, we will maximally the auger operation for the transportation and shearing of mass in the extruder or between cylinders

$$\varepsilon a < r < a,\ \varepsilon, a = \mathrm{const} > 0,\ \varepsilon < 1,$$

shifting it to the inner cylinder $r = \varepsilon a$, that, due to conditions of liquid particles sticking to it, now moves this mass along the axis z, at the same time as rotating it around this axis with a constant velocity of boundary displacement $w_- > 0$ and torsion $\upsilon_- < 0$, as in Fig. 2.23:

$$\begin{gathered} w|_{r=\varepsilon a} = w_-, w|_{r=a} = w_+, \upsilon|_{r=\varepsilon a} = \upsilon_-, \quad w_\mp, \upsilon_\mp = \mathrm{const}, \\ \text{where } w_- > 0, \quad \upsilon_- < 0 \text{ and } w_+ = \upsilon_+ = 0. \end{gathered} \tag{2.2}$$

Finally, assume that the incoming mass is pushed further with a constant gradient of excess pressure, or by the difference of its values $p_\pm$ at the ends of the chosen length:

$$-p_z = \frac{p_+ - p_-}{l} = \mathrm{const} > 0, 0 < z < l, p_- = p|_{z=0},\ p_+ = p|_{z=l}. \tag{2.3}$$

In the absence of mass forces and radial displacements of the liquid material rotating and being moved longitudinally by the auger, and more precisely, under the assumption that

$$u = 0,\ \upsilon = \upsilon(r),\ w = w(r)\,\text{and}\,g^r = g^z = 0, \tag{2.4}$$

the dynamic equilibrium (2.1) with conditions (2.2)–(2.4) is reduced to the proportions:

$$-\frac{1}{r}(rw_r)_r = \frac{-p_z}{\mu},\ (r\upsilon_r)_r = \frac{\upsilon}{r},\ p_r = \frac{p\upsilon^2}{r},\ -p_z = \frac{p_+ - p_-}{l}, \quad \varepsilon a < r < a,$$
$$0 < z < l,\ w(\varepsilon a) = w_-, w(a) = w_+ = 0,\ \upsilon(\varepsilon a) = \upsilon_-,\ \upsilon(a) = \upsilon_+ = 0,$$

or to Hagen–Poiseuille's flow between the pipes [26, 35],

$$w(r) = w_+ - \frac{p_z(a^2 - r^2)}{4\mu} + \left(w_- - w_+ + \frac{p_z a^2(1-\varepsilon^2)}{4\mu}\right)\frac{\ln\frac{r}{a}}{\ln\varepsilon} \text{ with } w_+ = 0,$$

at the same time spiral, as the Couette flow with azimuthal velocity

$$\upsilon(r) = \frac{\varepsilon a}{r}\frac{\upsilon_- - \varepsilon\upsilon_+}{1-\varepsilon^2} + \frac{r}{a}\frac{\upsilon_+ - \varepsilon\upsilon_-}{1-\varepsilon^2} = \frac{\varepsilon\upsilon_-}{1-\varepsilon^2}\left(\frac{a}{r} - \frac{r}{a}\right) \text{ with } \upsilon_+ = 0,$$

and with pressure falling along the radius to the center of rotation, as in a centrifuge [31]

$$p(r,z) = p_+ - \frac{z}{r}(p_+ - p_-) - \int_r^a \frac{\rho\upsilon^2(r')}{r'}\mathrm{d}r', l \quad p_r = \frac{\rho\upsilon^2}{r} > 0,$$
$$\varepsilon a < r < a, 0 < z < l.$$

In Fig. 2.24 in dimensionless variables of the radius X and speeds of displacement and rotation of auger, Z and Y,

$$\frac{4\mu w}{-p_z z^2} = Z = 1 - X^2 - \frac{1-\varepsilon^2-\delta}{\ln\varepsilon}\ln X, \quad 0 < \delta = \frac{4\mu w}{-p_z a^2} < 1 - \varepsilon^2,$$

and

$$\frac{\upsilon(r)}{\upsilon_-} = Y = \frac{\varepsilon}{1-\varepsilon^2}\left(\frac{1}{X} - X\right)$$

given the dependence of the latter from the first, i.e., dimensionless profiles $Z(X)$ and $Z(X)$ of the azimuthal $w(r)$ and axial $\upsilon(r)$ components of the velocity **u**. The latter depends on dimensionless parameters ε and δ: ratio of the inner radius $r_{\min}$ to an external a, or radial factor

$$\varepsilon = \frac{r_{\min}}{a},\ 0 < \varepsilon < 1,$$

and the ration of velocity of the boundary displacement w_- to the following speed viscous pressure w_p, or a dynamic factor

$$\delta = \frac{w_-}{w_p} = \frac{4\mu w_-}{-p_z a^2} > 0 \text{ at } w_p = \frac{-p_z a^2}{4\mu} \text{ and } -p_z > 0.$$

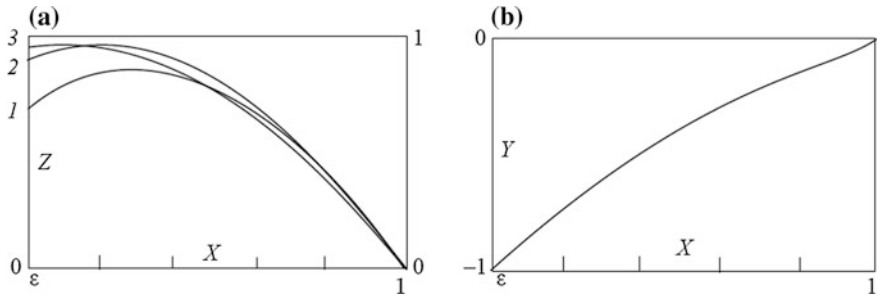

Fig. 2.24 Profiles of axial (left) and azimuthal (right) component of the considered spiral flow at two subcritical (1 and 2) and one supercritical (3) values of dynamic factor

Considered SVE extruders [30] are operated with the usually moderate values of $\varepsilon \approx 0.5$ and mostly at the subcritical value of $0 > \delta < 1 - \varepsilon^2$, rarely, at the supercritical factor $\delta > 1 - \varepsilon^2$, that is illustrated by the dimensionless dependence $Z(X)$ in Fig. 2.24, left.

At the subcritical dynamic factor and the maximum possible speed of material transportation by the auger $w(r)$ is limited by value

$$w_* = \max_{\varepsilon a \le r \le a} w(r) = w_p \max_{\varepsilon \le X \le 1} Z(X) = w(r_*),$$

close to the speed of viscous flow w_p, achieved within the field of flow: $\varepsilon a < r_* < a$. With the growth of the factor $\delta < 1 - \varepsilon^2$ this value approaches the speed w_p, shifting simultaneously on the internal radius of the cylinder $r = \varepsilon a$ and reaches w_p on the border of flow area, i.e., $r_* = \varepsilon a$ at $\delta = 1 - \varepsilon^2$, remaining maximum speed of the transported mass $w_* = w_p$ and at any superficial factor $\delta \ge 1 - \varepsilon^2$.

Thus, increasing the speed of displacement w_- at superficial factor δ does not increase the speed of transportation $w(r)$ in the flow area $\varepsilon a < r - a$, reaching the maximum value w_* on the border of this area $r_* = \varepsilon a$ and equal to the speed of viscous flow w_p.

The above concepts came from the central assumptions of continuum mechanics about the presence of the molecular pressure p in such materials and produced by its flow $\mathbf{u}$ liquid deformations $\mathbf{u_r} = (\nabla \mathbf{u})_*$, which together generate contact strain $\vec{\mathbf{p}}$, balancing the resulting acceleration of the particles in the Navier–Stokes Equations (2.1). The original premise of the mechanics of viscoplastic deformation seems to be the opposite: there is a solid body and the tension applied to its surface is defined as $\vec{\mathbf{p}}$ (Shear stress), which produce deformation $\mathbf{u_r}$ (Shear rate) upon reaching of a critical level—the so-called plasticity limit $\|\vec{\mathbf{p}}\| = const$ (Yield stress). But details of the dependence between tension and deformation are reduced to the above classical formula for $\vec{\mathbf{p}}$. The same viscoplastic state of the material is described by the above-mentioned dependence of dynamic viscosity $\mu = \mu(\gamma)$ on measure of deformations $\gamma = D[\mathbf{u}]$, reduced to the constant $\mu = const$ at the

superficial level of tension in well-known Bingham's model [28], which we also accept here for the flow of the material in extruder [36].

The mass is not only mixed, but also compressed. Therefore, we will consider in the simplified variant that

$$\rho = \rho(r) \neq \text{const}\,(\nabla \cdot \mathbf{u} \neq 0)\,\text{and}\,\mu = \text{const}.$$

Assuming that

$$u = u(r), \upsilon = \upsilon(r), w = w(r)\,\text{and}\,g^r = g^z = 0,$$

then the continuity equation in (2.1) leads to a permanent

$$r\rho u = m = \text{const}, \quad or\, ru = m\varphi,\ \text{where}\ \varphi = \frac{1}{\rho}$$

specific volume. When divided by dynamic viscosity,

$$\alpha = \frac{m}{\mu},$$

is a dimensionless value. Having in (2.1)

$$p_r = \frac{\rho\upsilon^2}{r}\ \text{and}\ \frac{\alpha+1}{r^2}(ru)_r - \left(\frac{1}{3}+\varsigma\right)\left(\frac{1}{r}(ru)_r\right)_r - \frac{1}{r}(ru)_{rr} - \frac{\alpha ru}{r^3} = 0$$

we solved for the values $\varphi_{\mp}$:

$$\varphi = \frac{\varepsilon^{\lambda_+}\varphi_+ - \varphi_-}{\varepsilon^{\lambda_+} - \varepsilon^{\lambda_-}}\left(\frac{r}{a}\right)^{\lambda_-} + \frac{\varepsilon^{\lambda_-}\varphi_+ - \varphi_-}{\varepsilon^{\lambda_-} - \varepsilon^{\lambda_+}}\left(\frac{r}{a}\right)^{\lambda_+},$$

$$\lambda_{\mp} = \frac{8+6\zeta+3\alpha}{2(4+3\zeta)} \mp \sqrt{\left(\frac{8+6\zeta+3\alpha}{2(4+3\zeta)}\right)^2 - \frac{3\alpha}{4+3\zeta}}\, at \left(\frac{8+6\zeta+3\alpha}{2(4+3\zeta)}\right)^2 > \frac{3\alpha}{4+3\zeta},$$

Satisfying the conditions (2.2)–(2.3) and Eq. (2.1)

$$\frac{m}{r}\upsilon_r + \frac{m\upsilon}{r^2} - \frac{\mu}{r}(r\upsilon_r)_r + \frac{\mu\upsilon}{r^2} = 0, \quad \frac{m}{r}w_r + \frac{mw}{r^2} - \frac{\mu}{r}(rw_r)_r = -P_z = -p_z,$$
$$P = p + \mu\left(\frac{2}{3}-\varsigma\right)\frac{1}{r}(ru)_r,\ \varepsilon a < r < a,$$

axial and azimuthal velocity components, in this case, have profiles:

$$w = \frac{\varepsilon^{\gamma_+}w_+ - w_-}{\varepsilon^{\gamma_+} = \varepsilon^{\gamma_-}}\left(\frac{r}{a}\right)^{\gamma_-} + \frac{\varepsilon^{\gamma_-}w_+ - w_-}{\varepsilon^{\gamma_-} - \varepsilon^{\gamma_+}}\left(\frac{r}{a}\right)^{\gamma_+}$$
$$+ \frac{-p_z a^2}{\mu(4-\alpha)}\left(\frac{\varepsilon^{\gamma_+} - \varepsilon^2}{\varepsilon^{\gamma_+} - \varepsilon^{\gamma_-}}\left(\frac{r}{a}\right)^{\gamma_-} + \left(\frac{\varepsilon^{\gamma_-} - \varepsilon^2}{\varepsilon^{\gamma_-} - \varepsilon^{\gamma_+}}\right)\left(\frac{r}{a}\right)^{\gamma_+} - \left(\frac{r}{a}\right)^2\right),$$

$$\gamma_{\mp} = \frac{\alpha}{2} \mp \sqrt{\left(\frac{\alpha}{4}-1\right)\alpha}\ at\ \left(\frac{\alpha}{4}-1\right)\alpha > 0,$$

Fig. 2.25 Raw brex exiting the extruder

and

$$\upsilon = \frac{\varepsilon^{\beta_+}\upsilon_+ - \upsilon_-}{\varepsilon^{\beta_+} - \varepsilon^{\beta_-}}\left(\frac{r}{a}\right)^{\beta_-} + \frac{\varepsilon^{\beta_-}\upsilon_+ - \upsilon_-}{\varepsilon^{\beta_-} - \varepsilon^{\beta_+}}\left(\frac{r}{a}\right)^{\beta_+},$$

$$\beta_\mp = \frac{\alpha}{4} \mp \left(\frac{\alpha}{2} + 1\right) = -\frac{\alpha}{4} - 1, \frac{3\alpha}{4} + 1.$$

The received analytical dependences allow one to qualitatively assess the flow of the formable mass in the extruder and can be used for further numerical simulation.

In zone 5, the brex are squeezed out of the holes in the die (Fig. 2.25), which completes the process of their formation.

2.4 The Length and the Cross-sectional Shape of Brex

The considerable length of the brex at the die exit is notable. In work [9], we carried out a finite-element simulation of exit of elongated brex from an extruder using the SIMULIA Abaqus software complex [37]. This modeling allowed us to offer a satisfactory description of the mechanism by which an elongated brex breaks into several brex of shorter length. When bending an elongated brex under the force of its own weight, zones of maximum stress and sources of further breakage are formed in its body. Figure 2.26 shows the results of mathematical modeling of the various stages of product breakage, both at the exit from the extruder and upon falling on the supporting surface (floor, conveyor belt, etc.).

In extrusion agglomeration, it is possible to produce brex of practically any shape by means of simply changing the shape of the orifice through which it passes in the die.

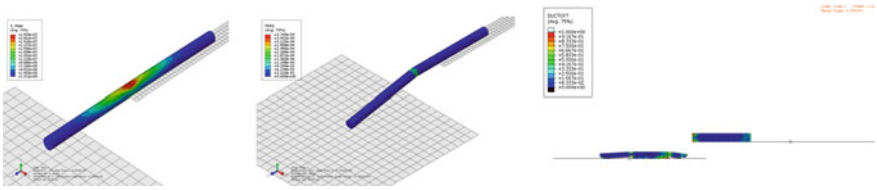

Fig. 2.26 Simulation of pressures in an elongated brex (on the left), its breakdown at the exit from the extruder (in the middle), and its falling onto a supporting surface (on the right)

Earlier, we investigated the effects of the shape of the brex on its strength [8]. Our experiment demonstrated that there was a significant difference in the strength between brex from the same batch depending on whether it has round or oval shapes. The strength of oval-shaped brex is dependent on the direction in which pressure is applied to it. When applying a crushing force along the minor axis of the oval, it may take almost twice as much pressure to achieve the same stress levels as it does when applying a pressure along the major axis. It can be assumed that the difference in the values of the strength can be attributed to the difference in the area of contact surface during crushing. For circular cross sections, the contact patch has a smaller area than it does for the oval samples if applied along the minor axis. Thus, when the load is equally distributed along the minor axis, the acting stresses in the oval-shaped brex are smaller than they are in the round shape. It is also clear that when the crushing force is directed along the major axis of the oval, the magnitude of stresses will be correspondingly higher. We performed a finite-element simulation of a full-scale brex-crushing experiment using the SIMULIA Abaqus software. The objects of our focus were brex of the same area with round and oval shapes. The ratio of the length of the major and minor axes of the oval is 2:1. Finite-element modeling was performed using a linear-elastic material model. As a result of mathematical modeling, we were able to evaluate the distribution of the equivalent von Mises stress over the cross section of the briquettes (Fig. 2.27). If the pressure required to split a round brex was 1, then the relative splitting pressures for an oval brex were 1.33 and 0.67 respectively along the minor and major axes.

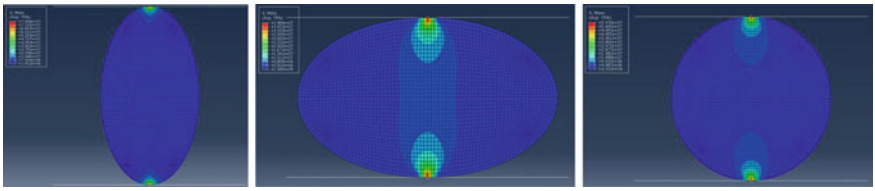

Fig. 2.27 Possible stresses on oval brex (left and middle) and circular cross sections, and the distribution of equivalent stresses in the body of the brex

2.5 Migration of Fines

Another feature of SVE is the possibility of extrusion of the fine fraction of the mixture during the production of brex on its surface, as illustrated by photos of brex made from a mixture of carbon-based material and construction fines (Fig. 2.28, left). It is evident that the carbon-based portion of the mixture formed the outer layer of the brex. The image on the right depicts coke brex bound by epoxy resin, the smallest particles of which are pushed out during the process of extrusion.

To understand the process that occurs when a mixture of large and small particles is moved, we proposed a simplified hydrodynamic model to describe the motion of large particles in a liquid. A similar model was developed for separating particles in dust-cleaning systems [38]. When applying the hydrodynamic model, we allowed for a simplification in which the fine phase is replaced by a liquid. In reality, the behavior of a fine solid phase differs from the behavior of a liquid, mainly because the solid phase is difficult to deform and does not flow as easily as a liquid, especially around obstacles. For a complete assessment, it is necessary to take into account the effect of particle shape and a number of other factors. However, for a general understanding of the principles of particle motion and of the forces that affect particles, such a simplification is permissible.

When the molded mass passes through the opening of die, we see a flow profile resembling that of the Poiseuille law on the flow of water through pipes (Fig. 2.29). A characteristic feature of such profiles is a large velocity gradient near the wall and a zero gradient at the center of the tube.

When finite-dimensional particles move in a gradient flow in an ordinary (Newtonian) environment, the resulting lift force is similar to that which acts on the wing of an aircraft. The latter occurs due to the difference in pressure under and above the wing of the aircraft ([26] and Fig. 2.30).

Fig. 2.28 Brex with a layer of fine fraction on the surface. Left: coal (surface layer) and fine fraction of construction materials. Right: coke brex with epoxy resin as binder

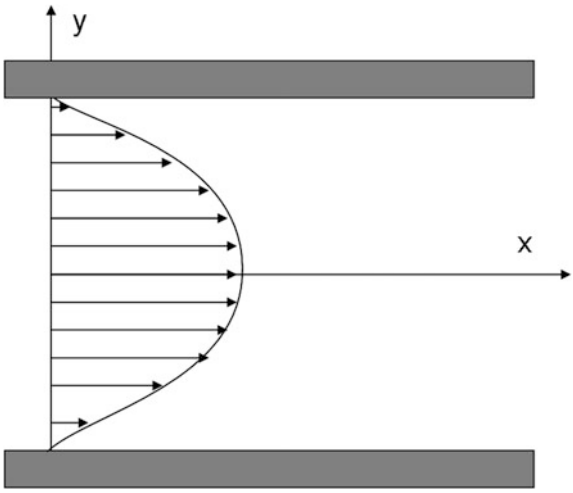

Fig. 2.29 Poiseuille flow profile

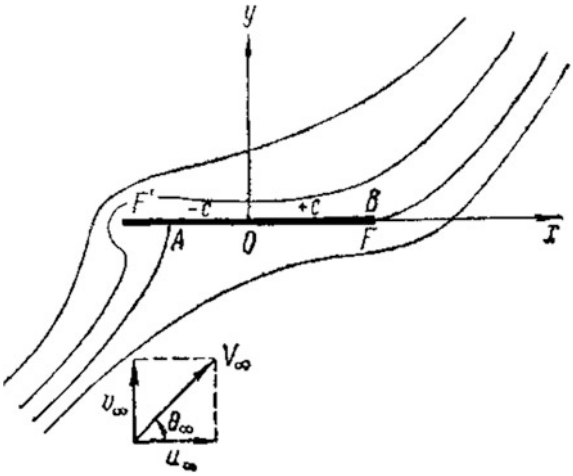

Fig. 2.30 Flow along the plate [26]

As per Bernoulli's principle, an ideal fluid of zero viscosity maintains pressure equal to the sum of its hydrostatic and dynamic pressures (the so-called Bernoulli integral) along its streamline [26].

$$p + \frac{\rho u^2}{2} = \text{const.} \tag{2.5}$$

Since air moves more slowly beneath the wing, the hydrostatic pressure must be greater to keep the Bernoulli integral (5) constant, with the reverse being true of the environment above the wing. For a particle in a flow with a velocity gradient (Fig. 2.31), an analogous situation arises: the pressure below the particle will be

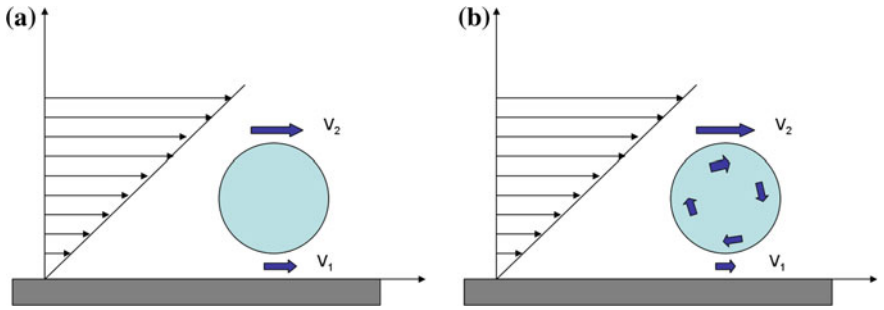

Fig. 2.31 **a** Flow around the particle near the wall extending from the hole; **b** The particle rotated by the flow

greater than it is above it. In this case, the particle may be pulled into rotation as a result of the velocity gradient. In this case, we will see a secondary lift force in the form of the Magnus effect, which surrounds a rotating particle (Fig. 2.31b).

As per Joukowski's theorem, lift is determined by the flow density ρ, circulation of velocity around the particle J, and the velocity of the oncoming flow u (the stream is assumed to have a horizontal velocity of u and a vertical velocity of $u = 0$) [26]:

$$F_{Magnus} = \rho J u \tag{2.6}$$

The circulation around the particle as it rotates in the flow is given by:

$$J = \frac{\pi r^2}{2} r \frac{\mathrm{d}u}{\mathrm{d}y} \tag{2.7}$$

where

πr^2 is a mid-length section of the particle,
r is the linear dimension of the particle,
$\mathrm{d}u/\mathrm{d}y$ is the velocity gradient of the flow (the y axis is directed vertically).

As a result, the Magnus force is proportional to the cube of the particle's volume, the velocity of the oncoming flow, and the velocity gradient [39]

$$F_{\text{Magnus}} \sim \rho \frac{\pi r^3}{2} u \frac{\mathrm{d}u}{\mathrm{d}y} \tag{2.8}$$

In reality, it is necessary to take into account that the particle is carried by the flow and has a horizontal velocity U (i.e., a relative velocity u–U). Therefore, we ultimately have the following:

$$F_{\text{Magnus}} = \rho \frac{\pi r^3}{2} (u - \text{U}) \frac{\text{d}u}{\text{d}y} \tag{2.9}$$

As can be seen from formula (2.9), the magnitude of the lift is larger for larger particles. Force also increases as the velocity gradient increases. The latter reaches its maximum value along the wall of a pipe, while amounting to zero at the center of the stream. Therefore, the greatest displacement of large particles toward the center will be observed near the wall, while the smallest particles being displaced toward the wall. As a result, there should be a nonuniform distribution of particles, with the largest ones at the center and the smallest ones near the wall.

When the particles move slowly relative to the "liquid" (in our case, relative to the fine phase), the Stokes' frictional force is observed [26]:

$$F_{\text{Stokes},x} = 6\pi\mu r(u - U), \tag{2.10}$$

where μ is dynamic viscosity (analogous to the friction of a small particle against a large particle), $(u–U)$ horizontal velocity relative to the flow.

Similarly, in the vertical direction, Stoke's frictional force is measured as:

$$F_{\text{Stokes},x} = 6\pi\mu r V, \tag{2.11}$$

where V is the vertical flow velocity relative to the object.

From the equilibrium of the Magnus force and Stokes's frictional force (where $F_{\text{Magnus}} = F_{\text{Stokes},y}$, y), we derive a formula for estimating velocity of the particle's transverse (vertical) displacement:

$$V = \frac{\rho}{12\mu} (u - \text{U}) \frac{\text{d}u}{\text{d}y} r^2 \tag{2.12}$$

This formula maintains that displacement velocity is proportional to the square of the particle size

Now we can make a qualitative assessment of the relative displacements of large and small particles. We can say that in (2.12) the difference $(u–U)$ characterizes the velocity of small particles relative to large particles. The velocity gradient du/dy is the same for small and large particles. Let us take, for example, the particles "large" and "small", where "large" is three times are large as "small" ($r_{\text{large}} = 3r_{\text{small}}$). Since $V \approx r^2$ and all other factors are equal, the transverse velocities of large and small particles will differ by a factor of nine.

$$V_{\text{large}} = -\frac{r^2_{\text{large}}}{r^2_{\text{small}}} V_{\text{small}} = -9V_{\text{small}}. \tag{2.13}$$

The "minus" sign is necessitated by the multidirectional motion of large and small particles in accordance with formula (2.12). In reality, we can assume that small particles remain in place and large ones are squeezed into the center of the stream.

The velocities of the relative transverse displacement of the particles are proportional to the square of the ratio of the particles' volumes.

The phenomenon of small fraction displacement is explained by the proposed hydrodynamic model using particles of two different sizes.

2.6 Transportation, Warehousing, and Storage of Brex

The high density of freshly made (green) brex enables them to be delivered immediately to the storage site by conveyor or loaded onto dump trucks (Fig. 2.32) for transport to the warehouse.

Due to the viscous or plastic reaction of a mass of brex to external mechanical action described in Sect. 3.1.—a reaction attributed to the granulometric composition of the mixture and the presence of bentonite—the brex show a sufficiently high impact strength. In the technological cycle of production of the brex for the smelting of ferromanganese (12.4% of aspiration dust from the production of ferromanganese, 40.8%—manganese containing sludge, 43.4%—screening of manganese pellets, and 3.4% bentonite as a binder) can withstand dropping from a height of 5 m onto the concrete floor of the bunker (Fig. 2.33).

Using the SIMULIA Abaqus software complex, it is possible to simulate the process of unloading oval-shaped brex in order to calculate the statistics surrounding the placement of brex on a pile (Fig. 2.34) [9]. Our results revealed that 56.25% of brex have a "flat" orientation (in which the long axis of an oval lies horizontally), 12.5% are oriented with the long axis perpendicular to the base, 12.5% are on the bottom, and 18.75% on the "edge." Thus, we were able to show that fewer than 13% of the brex in any given stack would lie in the direction in

Fig. 2.32 Loading of freshly formed brex onto a dump truck and its subsequent unloading 5 min later

Fig. 2.33 Unloading of green brex in the bunker with a height of over 5 m

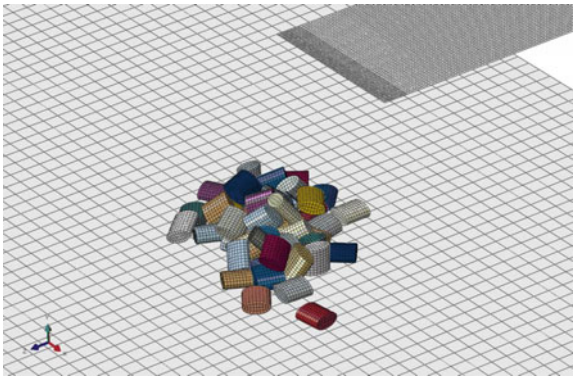

Fig. 2.34 Simulation modeling of placement of oval brex on the bed of the furnace

which the crushing force would theoretically be directed along the oval's long axis. We also noted that when an oval shape is formed, the free surface area increases (for brex with a 2:1 axis ratio, the surface area growth amounts to 5.8%), which would positively affect the process of its reduction in the reducing atmosphere.

In accordance with Russian standard 2787 (GOST 2787) [40], brex are dropped three times (freefall) from a height of 1.5 m onto a metal or concrete slab to determine their frailness. They should not generate more than 10% (mass) of fines. From every five brex dropped, four must pass the test. To simulate the process of brex breakage under impact loading, we evaluated the fall of brex onto an absolutely rigid flat surface from a height of 1.5 m. The specimens were then assessed from numerous angles: from the lateral surface, the front, and the edge (Fig. 2.35).

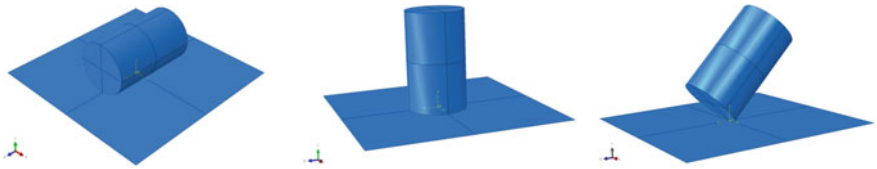

Fig. 2.35 Models of possible manners in which brex may fall onto a surface

The simulation was carried out using the elastic or plastic model for the brex behavior and keeping in mind the possibility of its destruction in the SIMULIA Abaqus software [41]. The physico-mechanical parameters of the material were determined by way of experimental data of the brex samples with a composition of 15% chromium ore concentrate, 15% coal, 67% aspiration dust resulting from ferrochrome production, and 3% Portland cement. In the experiment, the following properties of materials were noted using a bench-type single-column electromechanical Instron 3345 (USA) test machine with a loading capacity of 5 kN: a Young's modulus of 123 MPa, a Poisson's ratio of 0.3, and an ultimate strength 2.1 MPa. The results of the simulation are related in Figs. 2.36, 2.37 and 2.38. Results of simulations in which the brex fell from a height of 0.5 m and 2.0 m were also provided for the sake of comparing the damage parameter. The damage parameter is a conventional value characterizing the degree of material damage (0 for intact, 1 for completely destroyed). In the above simulation, regions of irreversible (inelastic) deformation were observed in contract zones in the body of the brex. A fall from a height of 0.5 m resulted in the complete destruction of the edge

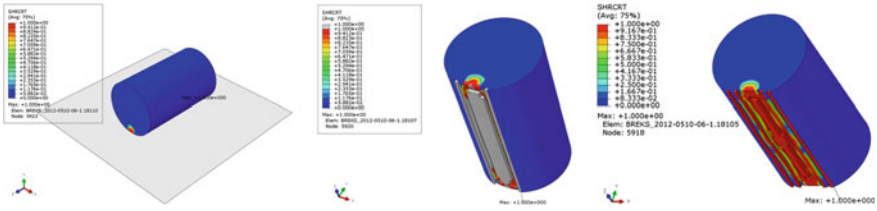

Fig. 2.36 The distribution of damage in a cylindrical-shaped brex. Type of impact: lateral surface. Height of the fall: 0.5 m (left), 1.5 m (middle), and 2.0 m (right)

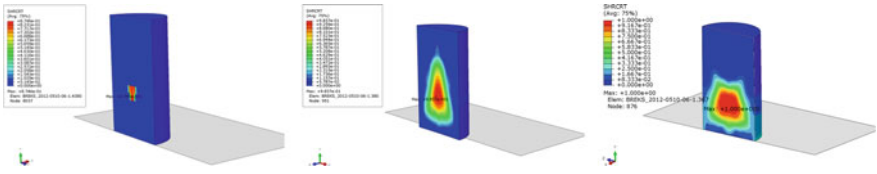

Fig. 2.37 The distribution of damage in a cylindrical-shaped brex. Type of impact: front. Height of the fall: 0.5 m (left), 1.5 m (middle), and 2.0 m (right)

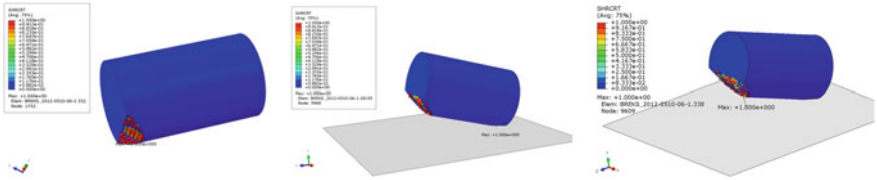

Fig. 2.38 The distribution of damage in a cylindrical-shaped brex. Type of impact: edge. Height of the fall: 0.5 m (left), 1.5 m (middle), and 2.0 m (right)

of the brex only if it were to fall onto its front. This is due to the small area of contact and a resulting higher degree of mechanical stresses in the model. In the remaining cases, the fall of brex led to an irreversible degradation of its strength in the contact zone without initiating the elements' progressive destruction. At a drop from a height of 1.5 m, the destruction of the brex's thin superficial layers was observed in practically all cases. It is worth noting that when brex falls onto its front (Fig. 2.37), damage (without destruction) is localized at its center. This is explained by the interference of compression-extension waves upon impact. The application of mathematical modeling to assess the destruction of brex under impact loading gives us an idea of the frailness of brex and allows us to predict its strength upon impact.

Figure 2.39 shows the results of sieving portions of brex No. 2 (Table 2.7) after the brex was dropped four times from a height of 1.5 m. The test produces an insignificant amount (less than 2%) of fines of less than 5 mm, as well as a single fragment exceeding 12.5 mm.

In accordance with Russian standard 25471-82 (GOST 25471-82) [42], in order to determine the durability of iron ores, agglomerates, and pellets upon impact, the materials must be subjected to a test of triple falls from a height of 2 m. A test of ore-sludge brex (consisting of 27% iron ore concentrate, 34% sludge, 32% dust, 6% Portland cement, and 1% bentonite) showed that fine formation did not exceed 2.7% after 48 h in the absence of a preliminary homogenization of the moldable mixture. In the presence of a preliminary homogenization, fine formation was at

Fig. 2.39 Test results for a four-time drop from a height of 1.5 m of brex No. 2

Fig. 2.40 Breaking of brex (after 48 h of preparation) after a five drops from a height of 2 m

2.1%. When the material was dropped five times, these values were at 5.6% for non-homogenized brex mixture and 3.7% for homogenized brex mixture (Fig. 2.40). These results were obtained 48 h after the brex were manufacture. It is known that the strengthening of the cement binders bonded briquettes is achieved upon a 16–20 h heat treatment or by means of natural strengthening (at a temperature of no less than 20 °C) for a period of 7 days [43]. An important feature of the SVE method is that, during the first 4 days of hardening, the brex show a viscous-plastic character during tests, which is evidenced by their high impact strength. Furthermore, as mentioned previously in this Chapter, within 48 h, cement-bentonite binder brex achieve a maximal local compressive strength.

One of the shortcomings of SVE that manifests itself in cold conditions is the need to maintain the temperature of the building in which the extrusion equipment is located at least 5 °C. Otherwise, the very extrusion of the wet mass will be difficult if not impossible, and, in the event that the mixture contains Portland cement, the hardening of the brex will slow down or cease entirely.

In order to estimate the temperature in a pile of freshly made brex over a 2-day period of storage, we sought to measure nonstationary heat conduction in the natural convective heat transfer with the environment, taking into account the physical heating of the brex during extrusion and ignoring the heat released during cement hydration.

Our variable was ambient temperature at 0, 5, and 10 °C. The initial temperature of the brex at the time of storage is 25 °C.

The thermophysical properties used are shown in Table 2.9.

The evaluation of the heat fields in the pile of brex was carried out over the course of 5 days (432,000 s) under unchanged external conditions. In accordance with the technological conditions of the SVE line operation for blast furnace unit, the brex are taken to charge after two days of storage.

Table 2.9 Thermophysical properties of materials

Material	Thermal conductivity, W/(m K)	Heat capacity, J/kg K	Density, k/m^3
Brex	10	620	2500
Air	0.026	1005	1.18

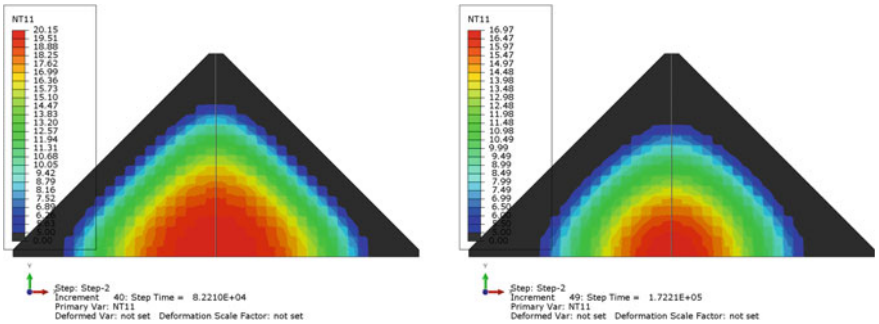

Fig. 2.41 Temperature field distribution. Day one is on the left-hand side; day two is on the right-hand side. The room temperature is 0 °C

Figure 2.41 shows the temperature distribution in the stack of brex at a room temperature of 0 °C after 24 and 48 h of storage.

Figure 2.42 shows the temperature distribution in the stack of brex at a room temperature of 5 °C after 24 and 48 h of storage.

Figure 2.43 shows the temperature distribution in the stack of brex at a room temperature of 10 °C after 24 and 48 h of storage.

Starting from a room temperature of 5 °C, the physical heat of the brex in the stack helps maintain sufficient temperatures for the hydration of cement. To verify the validity of this conclusion, we tested the durability of brex kept at 5 °C in a refrigeration chamber for 48 h by dropping them from a height of 2 m. The composition of this brex was as follows: 62.4% ore-sludge mixture, 30.6% blend of

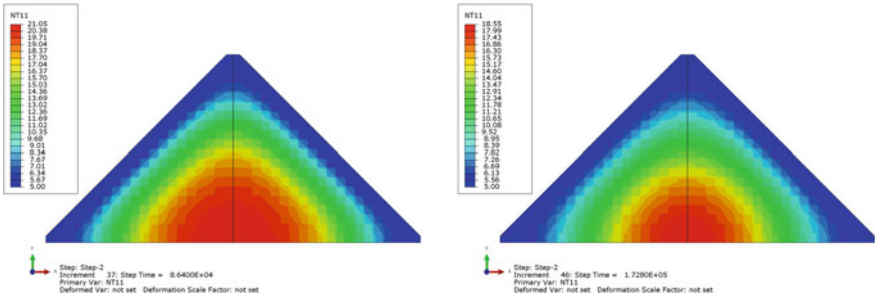

Fig. 2.42 Temperature field distribution. Day one is on the left-hand side; day two is on the right-hand side. The room temperature is 5 °C

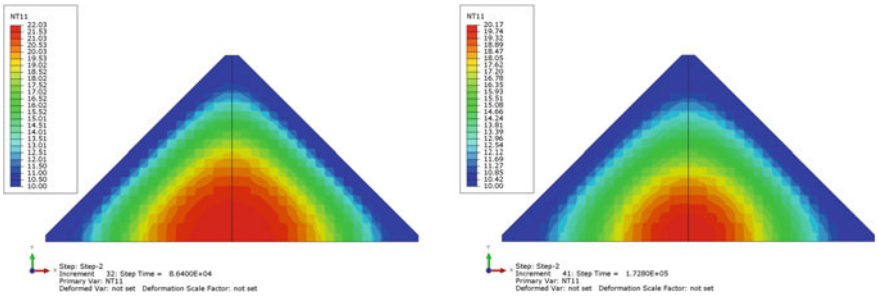

Fig. 2.43 Temperature field distribution. Day one is on the left-hand side; day two is on the right-hand side. The room temperature is 10 °C

blast furnace dust and dust resulting from aspiration, 6% Portland cement, and 1% bentonite. The amount of fines (particle less than 5 mm in size) formed after a three drop this the specified brex was 7% after 24 h of preparation at 5 °C, 4.3% after 48 h of preparation at 5 °C, and 4.2% after 72 h of preparation at 5 °C. If the brex are taken for charging into the blast furnace after 48 h of hardening at a room temperature of 5 °C, the strength of the brex is an acceptable level for use as blast furnace briquettes.

At temperatures close to zero, a significant number of brex will cool during the first 48 h to the temperatures at which hydration slows down or ceases entirely.

2.7 Conclusions

1. Allowing the briquetted material to develop plasticity is one of the most important aspects of preparing it for the production of brex. In many cases, it is sufficient to simply further grind the material. The method of grinding material for briquetting can affect the size, shape, and topography of the particle's surface. The degree to which these traits are affected depends on the features of the material (first and foremost on its porosity). The granulometric composition of briquetted material affects not only its compressive strength, but also determines the degree of damage that the brex will undergo under static and dynamic pressure. Depending on the degree of grinding, the fragility of the brex can be replaced with a viscous-plastic destruction, which will, in turn, increase the brex's resistance to impact.
2. Preliminary homogenization of a briquetted batch leads to an increase of its mechanical strength or to a decrease in the amount of binders and plasticizers necessary for its production. It is recommended to use a shearing extruder with a shearing plate to prepare the briquetted batch for homogenization.

3. The flow of a briquetted mass in the extruder is complex and not fully understood. The authors of this paper introduced a simplified model to assess the flow of a compressible mass in an extruder to obtain, for very first time, an exact analytic solution of the Navier-Stokes equations. This approach can be used as a template solution for numerical assessment. Practically all of the known results of mathematical modeling are based on the assumption that a medium is incompressible, which, actually, stands in conflict with the results of this study.
4. The mechanical strength of the brex is affected by their shape. Oval-shaped brex have a different splitting strength depending on the direction at which force is applied to them. The splitting force along the minor axis of the oval is great. The breakdown processes of elongated brex are well described using the SIMULIA Abaqus software, which is based on the finite elements method.
5. In a number of cases, the fines can be carried to the surface of the brex upon their productions. The same phenomenon is well noted in brick production through stiff extrusion. The authors proposed a hydrodynamic model to offer a satisfactory explanation of why a fine fractions may be displaced both in brex and brick production.
6. An analysis of the process of stacking the brex using SIMULIA Abaqus software allows you to model the distribution the brex by orientation in the stack. Knowledge of such distribution allows us to judge the effect of various crushing loads on the brex (axial compression, splitting during stretching).
7. Stiff extrusion agglomeration with the use of cement binder in combination with bentonite, leads to rather high values of impact strength of the brex already at the initial stage of strengthening. The formation of insignificant amounts of fines in brex after three drops from a height of 2 m after 48 h of preparation is due to the viscoplastic nature of their destruction in the first 4 days of strengthening.
8. The possibility of a stiff extrusion line operation on a cement binder is dependent on the necessity to keep the temperature in the room where the briquetting line is located at least 5 °C. Our study showed that after 48-hour strengthening of cement-based wet brex manufactured at 5 °C their drop-strength meet the requirements for blast furnace briquettes.

References

1. Bender, W., Haendle, F.: Brick and tile making, procedures and operating practice in the heavy clay Industries. Bauverlag GMBH, Berlin (1985)
2. Händle, F. (ed.): Extrusion in Ceramics, 468 C. Springer, Berlin (2007)
3. Gregory, R.: Briquetting coal without a binder. Colliery Guardian **201**, 5191 (1960)
4. Kaya, E., Glogg, R., Kumar, S.R.: Particle shape modification comminution. Kona **20**, 185–195 (2002)
5. Ulusoy, U., Hicyilmaz, C., Yekeler, M.: Role of shape properties of calcite and barite particles on apparent hydrophobicity. Chem. Eng. Process. **43**, 1047–1053 (2003)
6. Ulusoy, U., Yekeler, M., Hicyilmaz, C.: Determination of the shape, morphological and wettability properties of quartz and their correlations. Mineral Eng. **16**, 951–964 (2003)

7. Beirne, T., Hutcheon, J.M.: The shape of ground petroleum coke particles Brit. J. Appl. Phys. **13**, 576 (1954)
8. Bizhanov, A.M., Kurunov, I.F., Durov, N.M., et al.: Mechanical strength of BREX: Part I. Metallurg **7**, 32–35 (2012)
9. Bizhanov, A.M., Kurunov, I.F., Durov, N.M., et al.: Mechanical strength of BREX: Part II. Metallurg **10**, 36–40 (2012)
10. Malygin, G.A.: Plasticity and strength of micro—and nanocrystalline materials. Solid State Phys. **49**(6), 961–982 (2007)
11. Kawatra, S.K.: Effects of bentonite fiber formation in iron ore pelletization. Int. J. Miner. Process. **65**, 141–149 (2002)
12. Koizumi, H., Yamaguchi, A., Doi, T., Noma, F.: Fundamental development of iron ore briquetting technology. ISIJ **74**(6), 22–29 (1988)
13. Japan.: Patent S63196689 (A), (1988)
14. Bogdan, E.A., Cole, R.L.: US Patent 5395441, 1995
15. Hideo, K., Nobuhide, O.: Experimental study on swelling characteristics of compacted bentonite. Can. Geotech. J. **40**, 460–475 (2003)
16. Dvorkin, L.I., Dvorkin, O.L.: Building Mineral Binding Materials. Infra Inzheneriya, Moscow (2011)
17. Ozhogin, V.V.: Foundations of Theory and Technology of Briquetting of Pulverized Metallurgical Raw Materials: Monograph. PGTU, Mariupol (2010), 442p
18. Bulatov, A.I., Danishevskii, V.S.: Grouting Mortars. Nedra, Moscow (1987)
19. Jones, G.K.: Chemistry and flow properties of bentonite grouts. In: Proceedings of Symposium on Grouts and Drilling Muds in Engineering Practice, pp. 22–28. Butteworths, London (1963)
20. Shmit'ko, E.I., Krylov, A.V., Shatalova, V.V.: Chemistry of Cement and Binding Substances. Prospekt Nauki, St. Petersburg (2006)
21. Moroz, I.I.: Technology of Structural Ceramics. Ecolit, Moscow (2011), 384p
22. Ruzhinskiy, S., et al.: All about Foam Concrete. 2nd ed., improved and expanded. OOO Stroy Beton (Stroy Beton, LLC), St. Petersburg (2006), 630p
23. Bizhanov, A.M., Eriklintsev, I.V., Kozlov, S.A., Troshkin, O.V.: On Spiral Couette-Poiseuille Flow in Simplified Extruder Problem. J. Comput. Math. Math. Phys. (2017) (in print)
24. Händle, F., Laenger, F., Laenger, J.: Determining the Forming pressures in the extrusion of ceramic bodies with the help of the Benbow-Bridgwater equation using the capillar check. Process Eng. **92**(10–11), 1–7 (2015)
25. Batchelor, G.K.: An introduction to fluid dynamics. Cambridge University Press, Cambridge (1967), 615p
26. Loytsyanskiy, L.G.: Mechanics of Liquids and Gases. Science, Moscow (1987), 840p
27. Abramovich, G.N.: Applied Gas Dynamics. Part 1. Science, Moscow (1991), 600p
28. Bingham, E.C.: Fluidity and Plasticity. McCraw-Hill Book Company, Inc., New York, London (1922), 439p
29. Ishlinskiy, A.Y., Ivlev, D.D.: Mathematical Theory of Plasticity. Publishing House of Physical and Mathematical and Technical Literature, Moscow (2001), 704p
30. Laenger, K.-F., Laenger, F., Geiger, K.: Wall slip of ceramic extrusion bodies, Part 2. Process Eng. **93**(4–5), 1–6 (2016)
31. Belotserkovskiy, O.M., Betelin, V.B., Borisevich, V.D., Denisenko, V.V., Kozlov, S.A., Eriklintsev, I.V., Konyukhov, A.V., Oparin, A.M., Troshkin, O.V.: Toward theory of counterflow in rotating viscous heat-conducting gas. J. Comput. Math. Math. Phys. **51**(2), 222–236 (2011)
32. Troshkin, O.V.: Elements of Mathematical Hydrodynamics and Hydrodynamic Stability. ISBN-978-3-659-93972-3
33. Landau, L.D., Lifshitz, E.M.: Theoretical Physics V.7. Theory of Elasticity. Science, Moscow (1987), 248p

34. Galitskov, S.Y., Nazarov, M.A.: Simulation of Velocity Field of Shear Deformations of Ceramic Mass in Forming Unit of Screw Extruder. Fundamental Studies vol. 8. pp. 29–32 (2013)
35. Joseph, D.: Stability of Fluid Motions. World, Moscow (1981), 638p
36. Mitsoulis, E.: Flows of viscoplastic materials: models and computations. Rheology Reviews 135–178 (2007)
37. Electronic resource http://www.tesis.com.ru Abaqus User Manual, Version 6.12 Documentation
38. Sobolev, A.A., Melnikov, P.A., Tyutyunnik, A.O.: Movement of Particles in Air Stream, vol. 3, Issue No. 17, pp. 82–86. Vector of Science of Togliatti State University
39. Deryagin, B.V., Churaev, N.V., Muller, V.M.: Surface Forces. Science, Moscow (1985), 400p
40. GOST (All-Union State Standard) 2787–75 Metals Ferrous Secondary. General specifications
41. Bizhanov, A.M., Kurunov, I.F., Podgorodetskiy, G.S., Nushtaev, D.V.: Investigation of Mechanism of Brex Destruction under Static and Impact Loads, vol. 8. pp. 26–31. Metallurgist (2014)
42. GOST (All-Union State Standard) 25471-82 Iron Ores, Agglomerates and Pellets. Method for Determining Drop Strength
43. Dorofeev, G.A., Barsukova, E.A.: On the choice of rational method of agglomeration of fine materials of anthropogenic and natural origin. Ferrous Metall. **12**, 73–79 (2015)

http://www.springer.com/978-3-319-72711-0

Stiff Extrusion Briquetting in Metallurgy

Kurunov, I.; Bizhanov, A.

2018, XII, 169 p. 133 illus., 81 illus. in color., Hardcover
ISBN: 978-3-319-72711-0